

# Evidence for a Compact Object in the Aftermath of the Extra-Galactic Transient AT2018cow

**Dheeraj Pasham** (✉ [dheeraj@space.mit.edu](mailto:dheeraj@space.mit.edu))

Massachusetts Inst of Technology

**Wynn Ho**

Haverford College <https://orcid.org/0000-0002-6089-6836>

**William Alston**

ESA

**Ronald Remillard**

Massachusetts Inst of Technology <https://orcid.org/0000-0003-4815-0481>

**Mason Ng**

Massachusetts Inst of Technology

**Keith Gendreau**

NASA GSFC <https://orcid.org/0000-0001-7115-2819>

**Brian Metzger**

Columbia University

**Diego Altamirano**

Southampton University <https://orcid.org/0000-0002-3422-0074>

**Deepto Chakrabarty**

Massachusetts Inst of Technology

**Andrew Fabian**

University of Cambridge <https://orcid.org/0000-0002-9378-4072>

**Jon Miller**

University of Michigan

**Peter Bult**

NASA Goddard Space Flight Center

**Zaven Arzoumanian**

X-ray Astrophysics Laboratory, NASA Goddard Space Flight Center, Greenbelt, MD 20771

**James Steiner**

Center for Astrophysics | Harvard & Smithsonian

**Tod Strohmayer**

NASA/GSFC

**Francesco Tombesi**

Tor Vergata University of Rome

**Jeroen Homan**

Eureka Scientific, Inc. <https://orcid.org/0000-0001-8371-2713>

**Edward Cackett**

Wayne State University <https://orcid.org/0000-0002-8294-9281>

**Alice Harding**

Los Alamos National Laboratory

---

## Research Article

**Keywords:** Fast Blue Optical Transients (FBOTs), astrophysical phenomena, AT2018cow

**Posted Date:** May 10th, 2021

**DOI:** <https://doi.org/10.21203/rs.3.rs-465345/v1>

**License:**   This work is licensed under a Creative Commons Attribution 4.0 International License.

[Read Full License](#)

---

**Version of Record:** A version of this preprint was published at Nature Astronomy on December 13th, 2021. See the published version at <https://doi.org/10.1038/s41550-021-01524-8>.

<sub>1</sub> Evidence for a Compact Object in the Aftermath of the  
<sub>2</sub> Extra-Galactic Transient AT2018cow

3 Dheeraj R. Pasham<sup>1\*</sup>, Wynn Ho<sup>2</sup>, William Alston<sup>3</sup>, Ronald Remillard<sup>1</sup>,  
Mason Ng<sup>1</sup>, Keith Gendreau<sup>4</sup>, Brian Metzger<sup>5</sup>, Diego Altamirano<sup>6</sup>,  
Deepto Chakrabarty<sup>1</sup>, Andrew Fabian<sup>7</sup>, Jon Miller<sup>8</sup>, Peter Bult<sup>4,9</sup>,  
Zaven Arzoumanian<sup>4</sup>, James Steiner<sup>10</sup> Tod Strohmayer<sup>4</sup>,  
Francesco Tombesi<sup>4,9,11,12</sup>, Jeroen Homan<sup>13</sup>, Edward Cackett<sup>14</sup>, Alice Harding<sup>15</sup>

<sup>1</sup>Kavli Institute for Astrophysics and Space Research, Massachusetts Institute of Technology,  
Cambridge, MA 02139, USA

<sup>2</sup>Department of Physics and Astronomy, Haverford College, 370 Lancaster Ave,  
Haverford, PA 19041

<sup>3</sup>European Space Agency (ESA), European Space Astronomy Centre (ESAC),  
Villanueva de la Cañada, Madrid, E-28691, Spain

<sup>4</sup>NASA Goddard Space Flight Center, Greenbelt, MD, USA

<sup>5</sup>Columbia Astrophysics Laboratory, Columbia University, New York, NY 10027, USA

<sup>6</sup>Department of Physics and astronomy, University of Southampton,  
University Road, Southampton, SO17 1BJ, UK

<sup>7</sup>Institute of Astronomy, University of Cambridge, UK

<sup>8</sup>Department of Astronomy, 311 West Hall, 1085 South University Ave.,  
Ann Arbor, MI 48109-1107

<sup>9</sup>Department of astronomy, University of Maryland College Park, MD, 20742

<sup>10</sup>Center for Astrophysics, Harvard, Cambridge, MA

<sup>11</sup>Department of Physics, Tor Vergata University of Rome, Via della Ricerca Scientifica 1,  
00133 Rome, Italy

<sup>12</sup>INAF Astronomical Observatory of Rome, Via Frascati 33, 00040 Monte Porzio Catone, Italy

<sup>13</sup>Eureka Scientific, Inc., Oakland, CA 94602, USA

<sup>14</sup>Department of Physics and astronomy, Wayne State University, 2155 Old Main,  
4841 Cass Avenue, Detroit, MI 48201

<sup>15</sup>Theoretical Division, Los Alamos National Laboratory, Los Alamos, NM 87545

\*To whom correspondence should be addressed; E-mail: dheeraj@space.mit.edu

4 **Fast Blue Optical Transients (FBOTs) are mysterious extragalactic explosions**  
5 **that may represent a new class of astrophysical phenomena (*I*). Their fast**

6 time to maximum brightness of less than 10 days and decline over less than  
7 2 months and unusual optical spectra and evolution are difficult to explain  
8 within the context of core-collapse of massive stars which are powered by ra-  
9 dioactive decay of Nickel-56 and evolve slowly on months timescales (2, 3).  
10 AT2018cow (at a redshift of 0.014) is an extreme FBOT both in terms of rapid  
11 evolution and high X-ray and bolometric luminosities (4–7). Several alterna-  
12 tive hypotheses have been proposed to explain its unusual properties. These  
13 include shock interactions with dense circumstellar medium (5, 8, 9), tidal dis-  
14 ruption of a star by a  $10^{4-6}$  solar mass black hole (7, 10), a failed supernova  
15 with fallback accretion onto a newborn black hole (5), neutron star formed  
16 in a supernova (11) or from merging compact objects (12, 13), etc. Here, we  
17 present evidence for a high-amplitude (fractional root-mean-squared ampli-  
18 tude of  $>30\%$ ) quasi-periodic oscillation (QPO) of AT2018cow’s soft X-rays  
19 with a centroid frequency of roughly 225 Hz (statistically significant at the  
20  $3.7\sigma$  level, or a false alarm probability of 0.02%). This signal is found in the  
21 average power density spectrum of data taken over the entire outburst last-  
22 ing roughly 60 days and thus suggests that the signal is highly persistent over  
23 several hundreds of millions of cycles (60 days  $\times$  225 Hz). This high frequency  
24 (rapid timescale) of 225 Hz (4.4 ms) argues for the presence of a compact ob-  
25 ject in AT2018cow which can either be a neutron star or a black hole, and  
26 disfavors circumstellar medium interactions for the origin of X-ray emission.  
27 Also, the QPO’s timescale sets an upper limit on the compact object’s mass to  
28 be 850 solar masses, and thus disfavors models with a heavier black hole. If  
29 the QPO represents the spin period of a neutron star we can also set upper  
30 limits on its magnetic field under different scenarios. This work highlights a

31 **new way of using high time-resolution X-ray observations to study FBOTs.**

32 High-cadence sky surveys that can scan the same portions of the sky multiple times per night  
33 have uncovered a new class of fast-evolving optical transients (2, 3, 14). These "fast" transients  
34 rise to their peak brightness within  $\lesssim 10$  days and fade away within a month or two (e.g., (2)).  
35 They are spatially coincident with external galaxies but are offset from their nuclei (e.g., (2, 15)).  
36 Their optical spectra are often blue with occasional presence of Hydrogen and Helium features  
37 and are unlike any known class of supernovae (16). Their peak luminosities range from the  
38 faint end of core-collapse supernovae to the bright end of superluminous supernovae (see Fig.  
39 1 of (1)). Their fast rise times are difficult to reconcile with an origin from radioactive heating  
40 by  $^{56}\text{Ni}$  which produces light curves that evolve on much slower timescale of weeks to months  
41 (see, for example, Fig. 20 of (2)).

42 Thus, several alternate mechanisms have been proposed to explain the properties of these  
43 luminous Fast, Blue Optical Transients (FBOTs). These include emission from the interaction  
44 of the supernova shockwave with a dense circumstellar medium (e.g., (17)), injection of energy  
45 from spin down of a young magnetar formed either in a core-collapse supernova or a binary  
46 neutron star merger (e.g., (11, 13)), accretion onto a newly formed compact object in a failed  
47 supernova (e.g., (18)), mergers of binary white dwarfs (e.g., (19)), and intermediate-mass black  
48 holes (IMBHs: a few  $\times 10^{4-5} M_{\odot}$ ) tidally disrupting stars (7, 10). Given the diversity in their  
49 optical spectra evolution, peak brightness and total energy output, it is likely that they are a  
50 heterogeneous population.

51 Prior to June 2018, all bright FBOTs were first identified in archival images (e.g., (2, 15,  
52 20, 21)). AT2018cow, discovered by the ATLAS sky survey (22) in a galaxy at a distance of  
53  $\approx 60$  Mpc (6), was the first FBOT discovered in real time. Its brightness rise of more than 5.7  
54 magnitudes in just 4 days (see Fig. 1 of (6)) was remarkable and its peak bolometric luminosity  
55 of  $4 \times 10^{44} \text{ erg s}^{-1}$  makes it the brightest FBOT known so far (1). As the discovery was promptly

56 reported (23), the source received a significant amount of multi-wavelength coverage. Radio,  
57 millimeter, optical, UV, X-ray and gamma ray properties of the source are described in various  
58 papers (4–7, 10). However, in spite of exquisite coverage the physical origin of AT2018cow  
59 remains elusive.

60 Given its high X-ray luminosity (peak value of a roughly  $10^{43}$  erg/s, (5)) and variability on  
61 timescales of a few tens of hours (5), compact object (accretion) powered scenarios have been  
62 proposed for AT2018cow. These suggestions include emission from tidal disruption of a star by  
63 an intermediate-mass black hole with mass in the range of  $10^{4-6} M_{\odot}$  (7), fallback accretion in a  
64 failed supernova (5, 24), and energy injection by a newly born neutron star in a supernova (25).

65 Several works over the last few decades (26) have found that when accreting compact ob-  
66 ject (stellar-mass black hole/neutron star) X-ray binaries go into outbursts—due to enhanced  
67 accretion—they sometimes exhibit high-frequency (a few  $\times$  (10-100) Hz) quasi-periodic variabil-  
68 ity in their X-ray brightness. There is no clear consensus on the exact mechanisms that pro-  
69 duce these so-called High-Frequency Quasi-Periodic Oscillations (HFQPOs) but it is generally  
70 agreed upon that they originate from a region close to the compact object where the dynamics  
71 of motion are dictated by the compact object’s strong gravitational field (see (26) and refer-  
72 ences therein), and they represent a direct evidence for the presence of a compact object. More  
73 recently, analogous HFQPOs (frequencies of a few mHz) have also been found in stellar tidal  
74 disruption events involving  $\sim 10^6 M_{\odot}$  black holes (27–29) suggesting that, perhaps, such QPOs  
75 are universal among all compact object systems that undergo extreme changes in accretion.

76 To test these hypotheses for a compact object (accretion) powered scenario, we studied  
77 AT2018cow’s X-ray (0.25-2.5 keV) variability using an average power density spectrum de-  
78 rived from the entire monitoring data taken by the Neutron Star Interior Composition Explorer  
79 (*NICER*) on board the International Space Station. We find evidence for an X-ray QPO in the  
80 average PDS (left panel of Fig. 1). The QPO signal has a centroid frequency, full width half

81 maximum (FWHM) and a fractional root-mean-squared amplitude of  $224.4 \pm 1.0$  Hz,  $< 16$  Hz,  
82 and  $30 \pm 3\%$ , respectively. Using a rigorous Monte Carlo approach (see supplementary material,  
83 SM) that takes into account the nature of the underlying noise continuum and the search trials,  
84 we find the global false alarm probability of this signal to be  $\approx 2 \times 10^{-4}$  (or  $3.7\sigma$  equivalent for  
85 a normal distribution; see right panel of Fig. 1 and SM).

86 We rule out various instrumental and particle backgrounds as the origin for this QPO signal  
87 (See SM). Based on the long term light curves derived from *NICER* and Neil Gehrels *Swift*  
88 X-ray telescope, which has imaging capability (see top panel of Fig. 2), and late time *XMM-*  
89 *Newton* X-ray images of AT2018cow’s field of view, we also rule out a contaminating source as  
90 the origin of this QPO (see Fig. 3). Furthermore, over the last three years of *NICER* operations  
91 a signal of similar nature has never been found in any of the several dozens of other targets  
92 (see, for example, Fig. S8). Based on these tests, we conclude that the signal is consistent with  
93 originating from AT2018cow.

94 After establishing that the signal is statistically acceptable and ruling out an instrumental and  
95 a background origin, we extracted the QPO’s signal-to-noise as a function of the accumulated  
96 exposure (See Fig. S7 and supplementary movie S1). It is evident that the QPO’s strength  
97 increases gradually with increasing exposure. This suggests that the signal is persistent and  
98 present at some level throughout the  $\sim 2$  month monitoring period. Taken at face value, this  
99 suggests that it is stable over  $\sim 60$  days/ $4.44$  ms  $\gtrsim 10^9$  cycles. Interestingly, the mean slope of  
100 the curve in Fig. S7 also steepens around the same time (near day 17) when high-amplitude  
101 X-ray flares start to appear on days timescale (see the blue diamonds in the upper panel of Fig.  
102 2). Moreover, the fractional rms of the QPO jumps around day 17 which also coincides with  
103 the time when the optical spectrum of AT2018cow underwent dramatic changes (see (5) for  
104 details). We separated the total exposure into two epochs, before and after day 17. We extract  
105 an average PDS from each of these two time intervals and the QPO is fit with a Lorentzian. The

106 QPO’s fractional rms amplitude appears to be higher at later times (see bottom panel of Fig. 2).

107 The frequency of this QPO alone can set stringent constraints on the underlying physical  
108 mechanism producing X-rays in AT2018cow. The causality argument suggests that the physical  
109 size of an object producing this signal cannot be larger than the light crossing size, i.e., speed of  
110 light  $\times (1/225 \text{ s}) \approx 1.3 \times 10^8 \text{ cm}$ . This small size points us naturally towards a compact object  
111 and disfavors emission from shock interactions (5, 8). If that compact object is a black hole  
112 then assuming the emission originates from the innermost stable circular orbit allows us to set  
113 an upper limit on the black hole mass. These limits are  $95 M_{\odot}$  and  $850 M_{\odot}$  for a maximally  
114 prograde spinning (spin has the same direction as the material falling in) and a retrograde (vice  
115 versa) spinning black hole, respectively. A larger emission radius (in units of gravitational radii)  
116 would require the object to be even more compact. This rules out a heavy IMBH ( $\gtrsim 850 M_{\odot}$ )  
117 in AT2018cow (10).

118 HFQPOs with frequencies in the hundreds of Hz range have been seen in a handful of  
119 stellar-mass black holes with known dynamical mass estimates (26). They often appear in  
120 pairs with frequency ratio of 2:3 (26). In these systems it appears that the black hole mass  
121 scales inversely with the HFQPO frequency (see, for example, Fig. 4.17 of (26)). While the  
122 frequency, coherence and width of AT2018cow’s QPO are similar to HFQPOs of stellar-mass  
123 black holes, the observed fractional rms amplitude is high (25-45% compared to a few percent  
124 in stellar-mass black holes (26)), and a harmonic is not apparent here. Furthermore, the QPO’s  
125 energy dependence is also uncertain given our narrow X-ray band pass of 0.25-2.5 keV. Also,  
126 the absence of any red noise (even at lower frequencies, i.e., a few  $\times$  mHz; see Fig. S3) is unlike  
127 accreting X-ray binaries. All the stellar-mass X-ray binaries with HFQPOs are relatively highly  
128 inclined (26). Given AT2018cow’s high (a few  $\times 10^{42}$  erg/s) average X-ray luminosity beaming  
129 is likely present, and this points towards a low inclination for this system. Thus, given all these  
130 factors, it is unclear if a direct comparison can be made with HFQPOs of stellar-mass black

131 hole binaries. Nevertheless, if we assume the same scaling law applies and that 225 Hz is the  
132 fundamental harmonic, then the implied black hole mass in AT2018cow is  $\sim 4 M_{\odot}$ .

133 Alternatively, the compact object could be a neutron star with the QPO representing its spin  
134 rate of 225 Hz. Since the QPO has a width of  $< 16$  Hz, we can constrain a change in the spin  
135 rate during the 60 days of observation to be  $< 16 \text{ Hz}/60 \text{ d} = 3 \times 10^{-6} \text{ Hz s}^{-1}$ . The standard  
136 scenario for spin rate evolution of a non-accreting/isolated neutron star then implies an upper  
137 limit on the stellar magnetic field of  $\sim 2 \times 10^{13}$  G, and qualitatively similar constraints on  
138 magnetic field can also be set by considering, for example, evolution of the X-ray luminosity or  
139 accretion (see Section 3 in SM). The frequency and X-ray luminosity of the QPO are consistent  
140 with a young pulsar with a Crab-like magnetic field of a few times  $10^{12}$  G (depending on X-ray  
141 efficiency). Such a scenario cannot however explain the high luminosity during the early phases  
142 of AT2018cow, unless it underwent large magnetic field strength or orientation changes. The  
143 observed rapid luminosity drop after roughly 40 days (see Fig. 2 and also Fig. 4 of (5)) would  
144 also require changes, perhaps in the surrounding material leading to the loss of a clear line of  
145 sight to the pulsar or its X-ray reflections.

146 Within the bounds of a central engine being either a neutron star, stellar-mass black hole or a  
147 few hundred  $M_{\odot}$  black hole, the QPO presented here can be produced under different scenarios.  
148 For example, it has been proposed that a flare like AT2018cow could arise from young star  
149 clusters containing stellar-mass black holes (mass  $\sim 10 M_{\odot}$ ) tidally disrupting a main sequence  
150 star (30) or from fallback accretion of material in a failed supernova whose core collapses into  
151 either a neutron star or a stellar-mass black hole (7). In all these scenarios, such a QPO signal  
152 could be envisioned. The detection of a star cluster near or coincident with AT2018cow could  
153 help to differentiate between these models. The implications of this QPO for AT2018cow's  
154 existing models are summarized in Table 1.

155 In summary, we present evidence for a 225 Hz X-ray QPO persistent for billions of cycles

156 from AT2018cow statistically significant at the  $3.7\sigma$  level. Previous works (5) have suggested  
157 a compact object in AT2018cow based on X-ray variability on a few tens of hours timescale  
158 and also its X-ray spectral resemblance to some accreting systems. The detection of regular  
159 variations on millisecond timescale presented here provides the most direct way to infer the  
160 presence of a compact object, although it still remains unclear whether that compact object is a  
161 stellar-mass black hole or a neutron star. If AT2018cow originated from the death of a massive  
162 star, our findings represent the birth of a compact object in a supernova. Similar signals in future  
163 FBOTs could allow astronomers to study infant compact objects immediately after birth.

Table 1: Models for AT2018cow’s X-ray emission and their validity against the 225 Hz QPO reported here. This table can be considered as a modified extension of Table 2 of (5).

Model/class of models	References*	Consistent with QPO?	Notes
Shock interactions with circumstellar medium (CSM)	(4, 8)	No	CSM interaction could explain emission at other (non X-ray) wavelengths, i.e., optical and radio but inconsistent with rapid X-ray variability
An embedded internal shock formed from interaction with dense CSM	(5)	No	A compact embedded internal shock is, in principle, consistent with the size constraint provided by the 225 Hz QPO. However, all X-ray QPOs known thus far in literature are from compact objects. So an internal shock model is disfavored.
Accreting intermediate-mass black hole ( $\gtrsim 10^3 M_{\odot}$ )	(7, 10, 31)	No	Based on causality argument the compact object producing the QPO has to be less than $850 M_{\odot}$ (see main text)
Neutron star (formed from merging white dwarfs/Supernova)	(6, 12)	Yes	Constraints on magnetic field if the 225 Hz QPO represents the spin period. However, the persistence of the signal in a narrow frequency range is challenging to explain (see SM)
Stellar-mass black hole (accreting from outer layers of a failed supernova/tidally disrupting a star)	(7, 30, 32, 33)	Yes	The QPO frequency is similar to those often seen in known stellar-mass black holes but the X-ray luminosity, rms, and QPO’s stability are unlike any known stellar-mass black hole systems (see main text)

\*Not an exhaustive list. Also see references therein.

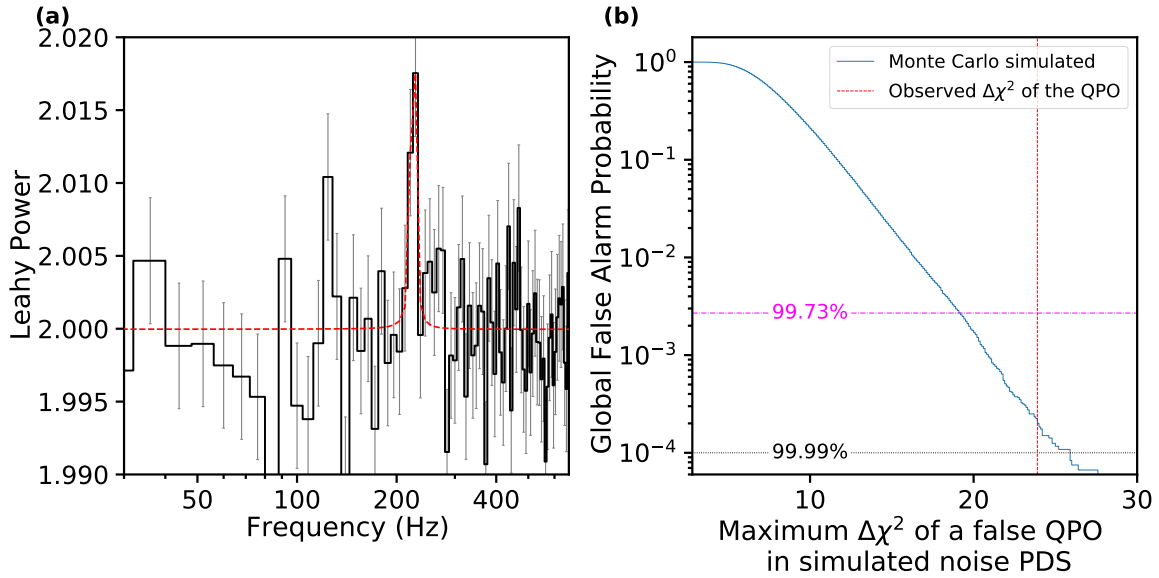


Figure 1: **(a) Average X-ray PDS of AT2018cow showing evidence for a quasi-periodicity near 225 Hz.** This PDS was computed by averaging 105 256-second soft X-ray (0.25-2.5 keV) light curves sampled at 1/2048 s. The resulting PDS was further re-binned by a factor of 2048 which gives a frequency resolution of 8 Hz. The strongest excess above the Poisson noise level of 2 is around 225 Hz. The power values in the rest of the PDS continuum are consistent with white noise (see SM sections 2.2.2 and 2.2 and Figures S2, S1, S3). The PDS is normalized such that the mean value surrounding 225 Hz is equal to the Poisson value of 2. The best-fit constant + Lorentzian models are indicated by dashed red curves. **(b) Estimates for the statistical significance of the 225 Hz QPO.** The likelihood of finding a QPO from noise fluctuations (y-axis) vs the maximum improvement in  $\chi^2$  by fitting the simulated noise PDS with a constant+Lorentzian over modeling it with a constant at every frequency searched during the identification of the signal on the left (see section 2.2.5 for more details). **The global false alarm probability of finding a QPO as strong as the one observed is  $\approx 2 \times 10^{-4}$  (1 in 5000;  $\approx 3.7\sigma$ ).**

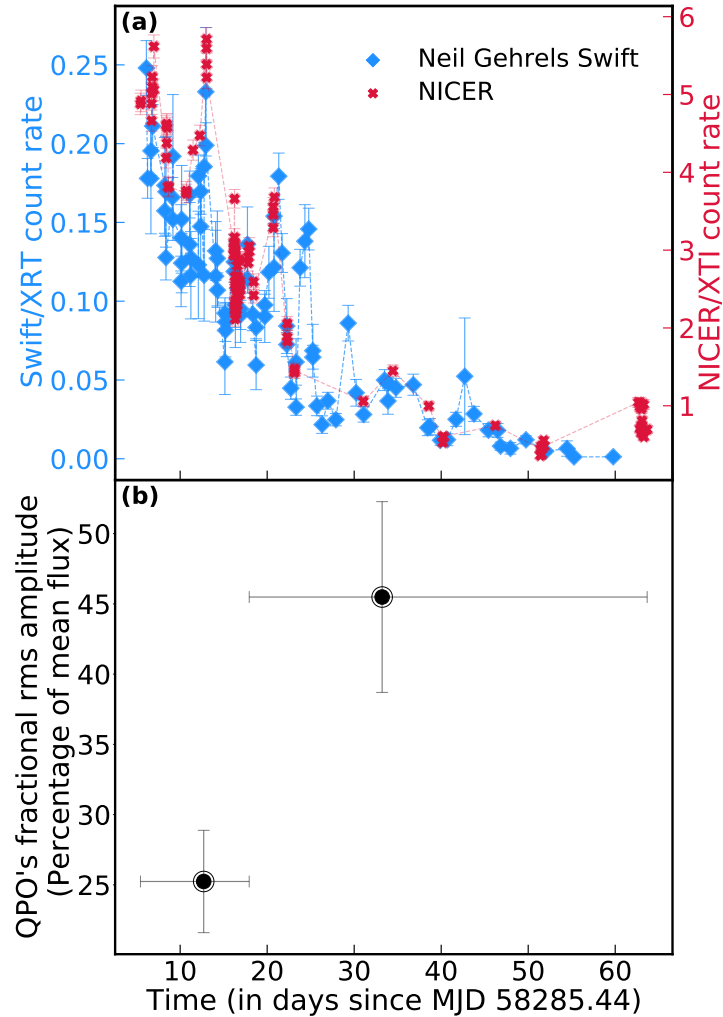


Figure 2: **(a) Comparison of *NICER/XTI* and Neil Gehrels *Swift/XRT* long-term light curves.** Both y-axes are in units of counts/sec. It is evident that AT2018cow’s long-term soft X-ray (0.25-2.5 keV) variability as observed by the non-imaging *NICER* telescope is same as that observed with Neil Gehrels *Swift/XRT* (0.3-2.5 keV) which has imaging capability. This suggests that the flux observed by *NICER* is dominated by AT2018cow with minimal contamination from other nearby astrophysical sources. **(b) Fractional root-mean-squared amplitude of the 225 Hz QPO vs time.** The signal appears to be stronger during the end of the outburst. The two values are  $25 \pm 4$  and  $45 \pm 7\%$  corresponding to exposures during  $12.7^{+5.2}_{-7.3}$  and  $33.2^{+30.5}_{-15.3}$  days, respectively. The jump in the QPO’s strength coincides with higher levels of variability on days timescale (XRT light curve in (a)) and also with the dramatic changes in optical spectra seen around the same time (5).

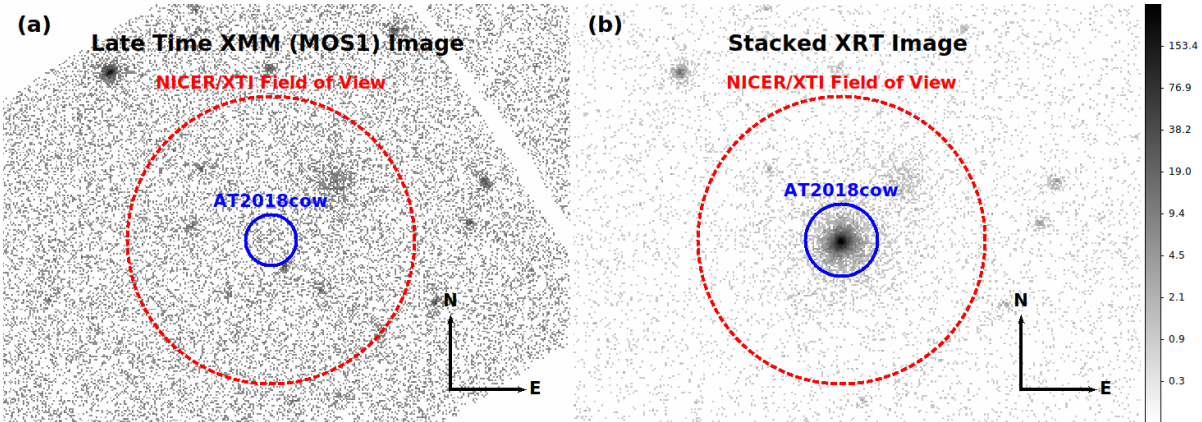


Figure 3: *XMM-Newton* and *Swift* images of *NICER*'s field of view of AT2018cow showing that there was minimal contamination from field sources. (a) *XMM-Newton*/MOS1 image of AT2018cow's field of view long after AT2018cow faded. The position of AT2018cow is indicated by a blue circle with a radius of 33". There is no contaminating point source directly coincident with AT2018cow. (b) Stacked Neil Gehrels *Swift*/XRT image of the field of view of AT2018cow. The blue circle of radius 47" is centered on AT2018cow's optical position (16:16:00.220 +22:16:04.91; J2000.0). This particular image was extracted by using all the archival XRT images as of July 2020. It is evident that while there are a few point sources present in *NICER*'s field of view, their contribution to overall XTI flux is negligible when compared to AT2018cow (see also Fig. 2). In both panels the outer/red (dashed) circles show *NICER*/XTI's approximate field of view of 3.1'. The north and east arrows are each 100" long. The colorbar show counts.

## References

- 164 1. C. Inserra, *Nature Astronomy* **3**, 697 (2019).
- 165 2. M. R. Drout, *et al.*, *Astrophys. J.* **794**, 23 (2014).
- 166 3. M. Pursiainen, *et al.*, *Mon. Not. R. Astron. Soc.* **481**, 894 (2018).
- 167 4. L. E. Rivera Sandoval, *et al.*, *Mon. Not. R. Astron. Soc.* **480**, L146 (2018).
- 168 5. R. Margutti, *et al.*, *Astrophys. J.* **872**, 18 (2019).
- 169 6. S. J. Prentice, *et al.*, *Astrophys. J.* **865**, L3 (2018).
- 170 7. D. A. Perley, *et al.*, *Mon. Not. R. Astron. Soc.* **484**, 1031 (2019).
- 171 8. S.-C. Leung, *et al.*, *Astrophys. J.* **903**, 66 (2020).
- 172 9. O. D. Fox, N. Smith, *Mon. Not. R. Astron. Soc.* **488**, 3772 (2019).
- 173 10. N. P. M. Kuin, *et al.*, *Mon. Not. R. Astron. Soc.* **487**, 2505 (2019).
- 174 11. D. Kasen, L. Bildsten, *Astrophys. J.* **717**, 245 (2010).
- 175 12. M. Lyutikov, S. Toonen, *Mon. Not. R. Astron. Soc.* **487**, 5618 (2019).
- 176 13. B. D. Metzger, A. L. Piro, *Mon. Not. R. Astron. Soc.* **439**, 3916 (2014).
- 177 14. M. Tanaka, *et al.*, *Astrophys. J.* **819**, 5 (2016).
- 178 15. A. Rest, *et al.*, *Nature Astronomy* **2**, 307 (2018).
- 179 16. A. V. Filippenko, *ARA&A* **35**, 309 (1997).
- 180 17. R. A. Chevalier, C. M. Irwin, *Astrophys. J.* **747**, L17 (2012).
- 181

- 182 18. K. Kashiwama, E. Quataert, *Mon. Not. R. Astron. Soc.* **451**, 2656 (2015).
- 183 19. J. Brooks, *et al.*, *Astrophys. J.* **850**, 127 (2017).
- 184 20. M. Tanaka, *et al.*, *Astrophys. J.* **819**, 5 (2016).
- 185 21. M. Pursiainen, *et al.*, *Mon. Not. R. Astron. Soc.* **481**, 894 (2018).
- 186 22. J. L. Tonry, *et al.*, *Publ. Astron. Soc. Pac.* **130**, 064505 (2018).
- 187 23. S. J. Smartt, *et al.*, *The Astronomer's Telegram* **11727**, 1 (2018).
- 188 24. E. Quataert, D. Kasen, *Mon. Not. R. Astron. Soc.* **419**, L1 (2012).
- 189 25. P. Mohan, T. An, J. Yang, *Astrophys. J.* **888**, L24 (2020).
- 190 26. J. E. McClintock, R. A. Remillard, *Black hole binaries* (2006), vol. 39, pp. 157–213.
- 191 27. D. R. Pasham, *et al.*, *Science* **363**, 531 (2019).
- 192 28. R. C. Reis, *et al.*, *Science* **337**, 949 (2012).
- 193 29. D. Lin, J. A. Irwin, O. Godet, N. A. Webb, D. Barret, *Astrophys. J.* **776**, L10 (2013).
- 194 30. K. Kremer, *et al.*, *arXiv e-prints* p. arXiv:2012.02796 (2020).
- 195 31. J.-H. Chen, R.-F. Shen, *Astrophys. J.* **867**, 20 (2018).
- 196 32. J. Dexter, D. Kasen, *Astrophys. J.* **772**, 30 (2013).
- 197 33. E. Quataert, D. Lecoanet, E. R. Coughlin, *Mon. Not. R. Astron. Soc.* **485**, L83 (2019).
- 198 34. K. C. Gendreau, *et al.*, *SPIE* (2016), vol. 9905 of *Society of Photo-Optical Instrumentation*  
199 *Engineers (SPIE) Conference Series*, p. 99051H.

- 200 35. N. Gehrels, *et al.*, *Astrophys. J.* **611**, 1005 (2004).
- 201 36. D. N. Burrows, *et al.*, *Space Sci. Rev.* **120**, 165 (2005).
- 202 37. F. Jansen, *et al.*, *Astron. Astrophys.* **365**, L1 (2001).
- 203 38. L. Strüder, *et al.*, *Astron. Astrophys.* **365**, L18 (2001).
- 204 39. G. Prigozhin, *et al.*, *SPIE* (2012), vol. 8453 of *Society of Photo-Optical Instrumentation*  
205 *Engineers (SPIE) Conference Series*, p. 845318.
- 206 40. M. van der Klis, *Timing Neutron Stars* (1988), vol. 262, pp. 27–70.
- 207 41. S. Vaughan, R. Edelson, R. S. Warwick, P. Uttley, *Mon. Not. R. Astron. Soc.* **345**, 1271  
208 (2003).
- 209 42. S. L. Shapiro, S. A. Teukolsky, *Black holes, white dwarfs, and neutron stars : the physics*  
210 *of compact objects* (1983).
- 211 43. B. D. Metzger, P. Beniamini, D. Giannios, *Astrophys. J.* **857**, 95 (2018).
- 212 44. V. F. Shvartsman, *Soviet Astronomy* **15**, 342 (1971).
- 213 45. A. F. Illarionov, R. A. Sunyaev, *Astron. Astrophys.* **39**, 185 (1975).
- 214 46. V. M. Lipunov, *Astrophysics of Neutron Stars* (1992).
- 215 47. K. Davidson, J. P. Ostriker, *Astrophys. J.* **179**, 585 (1973).
- 216 48. A. L. Piro, C. D. Ott, *Astrophys. J.* **736**, 108 (2011).
- 217 49. K. Parfrey, A. Spitkovsky, A. M. Beloborodov, *Astrophys. J.* **822**, 33 (2016).
- 218 50. M. A. Alpar, *Astrophys. J.* **554**, 1245 (2001).

219 51. S. M. Ransom, S. S. Eikenberry, J. Middleditch, *Astron. J.* **124**, 1788 (2002).

220 52. B. C. Andersen, S. M. Ransom, *Astrophys. J.* **863**, L13 (2018).

221 53. M. Bagchi, D. R. Lorimer, S. Wolfe, *Mon. Not. R. Astron. Soc.* **432**, 1303 (2013).

222 **Supplementary Materials.**  
223 Materials and Methods  
224 Figs. S1 to S8  
225 Caption for movie S1  
226 Movie S1  
227 Supplementary Text  
228 All the codes to download the data from HEASARC public archive, reduce it, and reproduce  
229 the results in this paper are available as supplementary files  
230

# Supplementary Material.

## 1 Data and Reduction.

The primary data used in this study was acquired by *NICER*'s X-ray Timing Instrument (XTI; (34)). We also utilized X-ray data from *Neil Gehrels Swift* observatory's (35) X-Ray Telescope (XRT; (36)) and *XMM-Newton*'s (37) European Photon Imaging Camera (EPIC; (38)). Below, we describe these data and their respective reduction methodologies in detail.

### 1.1 *NICER*/XTI:

The *NICER* X-ray observatory on board the International Space Station (ISS) has been carrying out full science operations since July 2017. XTI, which operates in the 0.25-12 keV band, is the primary instrument on *NICER* and it consists of 56 co-aligned X-Ray Concentrators (XRC). Each XRC focuses X-rays into an aperture of a Focal Plane Module (FPM) which consists of a single pixel (non-imaging) Silicon Drift Detector (SDD; (39)). At the beginning of science operations, 52 of the 56 FPMs were operational and together they provide an effective area of roughly 1900 cm<sup>2</sup> at 1.5 keV. This large effective area in the soft X-ray band combined with its ability to provide an absolute time resolution of better than 300 nanoseconds makes *NICER* a unique facility to detect the fastest known soft X-ray astrophysical signals.

*NICER* started monitoring AT2018cow roughly five days after its discovery in the optical band on MJD 58285.44 (6, 23)\*. In total, 26 sets of observations were made between MJD 58290.87 and 58349.11 with observation IDs running between 1200250101 and 1200250126. These datasets were publicly available and we downloaded them from the HEASARC archive<sup>†</sup>. The cleaned events lists were extracted using the standard *NICER* Data Analysis Software (NICERDAS/HEASoft 6.28) tasks `nicercal`, `nimpumerge`, and `nicerclean`. The latest *NICER* calibration release `xti20200722` (22 July 2020) was used. The cleaned event files were barycenter-corrected using the `barycorr ftools` task. AT2018cow's optical coordinates (J2000.0): (244.000917, +22.268031) were used along with `refframe=ICRS` and `ephem=JPLEPH.430`. The Good Time Intervals (GTIs) were extracted with the `nimaketime` tool using the default filters: `nicersaafilt=YES`, `saafilt=NO`, `trackfilt=YES`, `ang_dist=0.015`, `st_valid=YES`, `elv=30`, `br_earth=40`, `cor_range=""`, `min_fpm=38`, `underonly_range=0-200`, `overonly_range="0.0-1.0"`, `overonly_expr="1.52*COR_SAX**(-0.633)"` Conservative `elv=30` and `br_earth=40` were used to avoid optical loading by reflected light.

Due to a combination of decreasing effective area and increased contribution from high-energy particles the signal-to-noise (source-to-background) at energies  $\gtrsim 2.5$  keV deteriorates for faint X-ray targets like AT2018cow. Therefore, to minimize the contribution from the highly variable particle background, which is particularly important for variability studies, we only

\*Throughout this paper we refer times with respect to this optical discovery date

<sup>†</sup><https://heasarc.gsfc.nasa.gov/cgi-bin/W3Browse/w3browse.pl>

265 considered X-ray events in the energy range of 0.25 to 2.5 keV. This background cannot be di-  
266 rectly subtracted from the light curves, and thus acts to increase the noise in the power density  
267 spectra of the source. These are tested in detail in section 2.3. Our entire download and reduc-  
268 tion procedure can be easily replicated by running the codes that are available in supplementary  
269 files.

## 270 **1.2 Neil Gehrels *Swift*/XRT:**

271 Neil Gehrels *Swift* started monitoring AT2018cow on MJD 58288.44, roughly 3 days after its  
272 optical discovery. The observing cadence varied over the 58 d window coincident with the  
273 *NICER* observing campaign, i.e., until MJD 58349. For the first  $\approx 3$  weeks, Neil Gehrels *Swift*  
274 observed AT2018cow 3-4 times per day and thereafter the cadence was reduced to roughly one  
275 exposure per day. The individual exposure duration varied between 200 and 2000 s. In this  
276 work we only used XRT data in the band pass of 0.3-2.5 keV to be consistent with *NICER*'s  
277 energy range.

278 We started our analysis with the publicly available, raw, level-1 data from HEASARC  
279 archive and reprocessed them with the `xrtpipeline` task of HEASoft. Initially, when the  
280 source was bright, data was taken in both the Windowed Timing (WT) and the Photon Counting  
281 (PC) modes. But as the source count rate dropped observations were only carried out in the  
282 PC mode. For this work, we only used the PC mode data with event grades between 0 and 12.  
283 Source events were extracted from an annular region centered on AT2018cow with the outer ra-  
284 dius fixed at  $47''$ . This outer radius of  $47''$  corresponds to roughly 90% (at 1.5 keV) of the light  
285 from a point source (as estimated from XRT's fractional encircled energy function). The inner  
286 radius was determined independently for each exposure by accounting for pile-up using the for-  
287 malism described in the XRT user guide<sup>‡</sup>. Background events were extracted from an annular  
288 region centered on AT2018cow with an inner and outer radii of  $150''$  and  $210''$ , respectively.  
289 These values were chosen to avoid any point sources in that background annulus.

## 290 **1.3 *XMM-Newton*:**

291 *XMM-Newton* observed AT2018cow on three separate occasions roughly 37 (obsID:  
292 0822580401; 33 ks), 82 (obsID: 0822580501; 45 ks), and 218 days (obsID: 0822580601; 56  
293 ks) after its optical discovery. In this work, we only used the European Photon Imaging Camera  
294 (EPIC) data from the first and the last *XMM-Newton* epochs. The first exposure coincided with  
295 the *NICER* monitoring campaign while the last one was taken several months after AT2018cow  
296 faded away. As the data were taken in the *full frame mode* the Nyquist frequencies of the pn  
297 and MOS detectors were 6.8 Hz and roughly 0.2 Hz, respectively. To constrain the nature of  
298 variability on frequencies of a few Hz we only used pn data from the first dataset. For the last  
299 exposure MOS1 provides the best spatial resolution and hence we used only MOS1 data.

---

<sup>‡</sup><https://www.swift.ac.uk/analysis/xrt/pileup.php>

300 We started *XMM-Newton*/EPIC data reduction with the raw Observation Data Files (ODF)  
301 and reprocessed them using the XMM Science Analysis Software’s (xmmcas version 17.0.0)  
302 tasks `epproc` and `emproc` for the pn and MOS data, respectively. We employed standard  
303 data filters of ( $PATTERN \lesssim 12$ ) and ( $PATTERN \lesssim 4$ ) for the pn and the MOS data, respectively.  
304 We only considered events in the soft X-ray band of 0.25-2.5 keV to be consistent with *NICER*’s  
305 data (see section 1.1). We removed intervals of background flaring by manually inspecting the  
306 10-12 keV light curve as outlined in the XMM-Newton data analysis guide. The source count  
307 rates were extracted from a circular region of radius 33” which corresponds to 90% of the  
308 light from a point source as estimated by the fractional encircled energy of EPIC instruments.  
309 Background events were extracted from two nearby circular regions of radius 50”.

## 310 **2 Analysis**

### 311 **2.1 *NICER* identifies a QPO candidate**

312 We first divided the *NICER* data into 256-s continuous segments and extracted their light curves  
313 with a time resolution of 1/2048 s. This resulted in a total of 105 light curve segments, i.e., a  
314 cumulative exposure time of 26,880 s. With the mean count rate varying between 5.7 and 0.4  
315 count s<sup>-1</sup> this choice of 256 s ensured  $\gtrsim 100$  counts in each segment. A Leahy normalized  
316 (Poisson noise level of 2) power density spectrum (PDS) was extracted from each of these  
317 individual light curves and they were all combined to obtain an average PDS (see the left panel  
318 of Fig. 1). The PDS is consistent with a value of 2 (Poisson noise level) at all frequencies except  
319 for excess around 225 Hz.

### 320 **2.2 Estimating the global statistical significance**

321 To estimate the global false alarm probability of this QPO candidate near 225 Hz by properly  
322 accounting for the underlying noise and also all the search trials we devised a Monte Carlo ap-  
323 proach. The basic idea is to simulate a large number ( $\sim 10^5$  in our case) of random realizations  
324 of the underlying noise process, i.e., light curves that capture the underlying PDS continuum.  
325 Then, extract a power spectrum just like the real data, perform a global search (at all frequen-  
326 cies) for QPOs, and finally, estimate the probability of seeing a noise fluctuation that resembles  
327 a QPO as strong as the one found in the real data (left panel of Fig. 1). Because a robust sig-  
328 nificance estimate relies on accurate knowledge of the underlying noise process, at first, we lay  
329 extra emphasis on understanding the nature of the PDS continuum.

#### 330 **2.2.1 Probability plot: a qualitative assessment of noise**

331 Visually, the power spectrum in Fig. 1 appears to be flat (or white) between a few Hz to 1024  
332 Hz, except for the bins surrounding the QPO feature at 225 Hz. Formally, a test for flatness  
333 or “whiteness” of a power spectrum is a test for whether the power spectral values are  $\chi^2$

334 distributed (40). First, we assess this qualitatively by extracting a so-called probability plot.  
 335 It shows the theoretical quantiles of an assumed distribution ( $\chi^2$  with  $2 \times 105 \times 2048$  degrees of  
 336 freedom (dof) scaled by a factor of  $1/(105 \times 2048)$  in the present case) against the ordered sample  
 337 values, i.e., observed noise powers. This particular  $\chi^2$  distribution was used to compare because  
 338 the PDS in the left panel of Fig. 1 was obtained by averaging 105 individual PDS followed by  
 339 further averaging in frequency by a factor of 2048. If the observed data fall on a straight line on  
 340 the probability plot then that indicates that they are consistent with the theoretical distribution  
 341 that they are compared against. To remove the bias from the QPO we removed bins whose  
 342 frequencies fall between 200 and 250 Hz. Also because we are really only interested in the  
 343 nature of the noise continuum in the vicinity of 225 Hz we removed bins with frequencies  
 344 above 600 Hz. Because there are many bins between 600 and 1024 Hz they could, in principle,  
 345 skew the results. It is evident from Fig. S1 that the data points on the probability plot roughly  
 346 follow a straight line (red line) and thus appear “qualitatively” consistent with a  $\chi^2$  distribution  
 347 with  $2 \times 105 \times 2048$  dof scaled by a factor of  $1/(105 \times 2048)$ . For completeness, we repeated this  
 348 by considering all bins between 1/256 Hz and 1024 Hz and the result is the same.

### 349 **2.2.2 PDS continuum is consistent with White noise**

350 To investigate the nature of the PDS continuum quantitatively, we performed the Kolmogorov-  
 351 Smirnov (K-S) and the Anderson-Darling goodness-of-fit tests under the null hypothesis that  
 352 the PDS continuum is white, i.e., the power values between 1/256 and 600 Hz, except for bins  
 353 between 200-250 Hz, are  $\chi^2$  distributed with  $2 \times 105 \times 2048$  dof scaled by a factor  
 354 of  $1/(105 \times 2048)$ . The basic idea with these statistics is that they measure the maximum devi-  
 355 ation between the Empirical Distribution Function (EDF) of the data and that of a comparison  
 356 distribution. Therefore, the better the distribution fits the data, the smaller these statistics will  
 357 be.

358 Before we evaluated the K-S and Anderson-Darling test statistics we computed the EDF and  
 359 the probability density function (PDF) of the continuum noise powers. These are shown in the  
 360 top two panels of Figure S2) along with the expected EDF and PDF curves for a  $\chi^2$  distribution  
 361 (solid red). Similar to the probability plot, the data appear to track the expected  $\chi^2$  distribution  
 362 quite well.

363 We computed the K-S statistic using the EDF. To evaluate whether this value can be used  
 364 to reject or not reject the null hypothesis, we calculated the distribution of K-S statistic values  
 365 of EDFs drawn from the expected distribution:  $\chi^2$  with  $2 \times 105 \times 2048$  dof scaled by a factor of  
 366  $1/(105 \times 2048)$ . We compute this K-S statistic distribution as follows.

- 367 1. First, we randomly draw 57 values from a  $\chi^2$  with  $2 \times 105 \times 2048$  dof. Here, 57 refers  
 368 to the total number of power spectral continuum values between 100 and 600 Hz and  
 369 excluding those with frequencies between 200 and 250 Hz.
- 370 2. Then we evaluate the EDF of this random sample of 57 and scale it by  $1/(105 \times 2048)$
- 371 3. Finally, we compute its K-S statistic value.

372 The above steps are repeated 10,000 times to get a distribution of the K-S test statistic for a  
 373  $\chi^2$  distribution with  $2 \times 105 \times 2048$  dof for a given sample size of 57. This is shown as a blue  
 374 histogram in the bottom left panel of Fig. S2. AT2018cow’s observed K-S test statistic (dashed  
 375 vertical red line), which is a measure of maximum deviation between the observed EDF and  
 376 the theoretical Cumulative Distribution Function (CDF), is lower than the typical value (solid  
 377 magenta vertical line). This indicates that the null hypothesis cannot be rejected even at the 90%  
 378 confidence level and suggests that noise powers in the PDS continuum are very much consistent  
 379 with the expected  $\chi^2$  distribution, i.e., *NICER*’s PDS continuum is consistent with being white  
 380 between 1/256 and 1024 Hz.

381 To ensure the above conclusion is not dependent on the choice of the statistic used we also  
 382 computed the Anderson-Darling statistic. Similar to above, we computed its distribution using  
 383 bootstrap simulations (see the bottom right panel of Fig. S2). Again, it is clear that the statistic  
 384 computed from the observed PDS of AT2018cow (vertical dashed red line) is consistent with  
 385 the expected  $\chi^2$  distribution. We repeated all the above tests by considering all the bins between  
 386 1/256 to the Nyquist frequency of 1024 Hz (excluding those between 200-250 Hz) and the  
 387 results remained the same. We also varied the frequency upper limit from 400 Hz to 800 Hz  
 388 and they all yield the same result.

### 389 2.2.3 Modeling the PDS

390 Next, we carried out a straightforward method to test for flatness of the PDS continuum. We fit  
 391 the continuum, i.e., excluding the bins between 200 and 250 Hz, with two different models: a  
 392 constant (white noise) and a constant + power-law (white + red noise). The model consisting  
 393 of just a constant gave a  $\chi^2$  of 129.9 with 121 dof while the constant+power-law yields a  $\chi^2$  of  
 394 125.1 with 119 dof. We repeated this exercise with a PDS frequency resolution of 1/256 Hz,  
 395 i.e., lowest frequency of 1/256 Hz. This also did not yield in significant  $\chi^2$  improvement. This  
 396 argues that a power-law component is not formally required by the data.

397 Then we modelled the entire PDS (including the QPO bins) with a constant and a constant  
 398 plus a Lorentzian to account for the QPO feature. While the former yielded a  $\chi^2$  of 153.6  
 399 with 127 dof, adding a Lorentzian improved the  $\chi^2$  by 23.9, i.e., resulted in a  $\chi^2$  of 129.8 with  
 400 124 dof. This measurement forms the basis for our Monte Carlo simulations described in the  
 401 following sections. The best-fit QPO centroid is  $224.4 \pm 1.0$  Hz respectively.

402 The ratio of the sum of all the power values within the QPO width to error on that sum  
 403 gives a quick estimate of the signal-to-noise of the QPO. For the 225 Hz feature this value  
 404 is  $0.0295/0.0061 = 4.8$ . Combined with the mean source count rate of  $2.62 \pm 0.01$  counts/sec,  
 405 these values can also be used to estimate the fractional root-mean-squared (rms) amplitude of  
 406 the QPO to be  $100 \times \sqrt{0.0295 * 8 / 2.62} = 30 \pm 3\%$  (8 Hz is the frequency resolution here).

#### 2.2.4 Confirming white noise at lower (mHz) frequencies using longer/continuous light curves from *XMM-Newton*

To ensure that AT2018cow’s soft X-ray PDS is consistent with white noise at lower frequencies, i.e.,  $10^{-3}$ - $10^{-2}$  Hz we used a  $\sim 30$  ks *XMM-Newton* exposure that coincided with *NICER* monitoring. *NICER* data are not ideal for sampling at these low frequencies because of short exposures. We extracted an average 0.25-2.5 keV *XMM-Newton* PDS to find that there is no evidence for red noise down to in the frequency range of  $\sim 10^{-3}$  - a few Hz. The EPIC-pn PDS with a Nyquist frequency of 6.8 Hz is shown in Fig. S3.

Also, if there is strong red noise at low frequencies (or long timescales) that can manifest as variability on faster timescales. This effect is known as red noise leakage (41). In the present context, this means that if there is strong red noise below 1/256 Hz, that can, in principle, leak into the 100s of Hz range. The PDS in Fig. S3 also shows that the red noise leakage affect is negligible.

Based on all the above described tests and Figs. S1, S2 and S3 we conclude that over the frequency range of 1/256 to 1024 Hz the effect of red noise is negligible and that the PDS is consistent with being white.

#### 2.2.5 Monte Carlo Simulations to Estimate Global Statistical Significance

When the potential signal you are trying to test for is broad and distributed over several frequency bins, the standard approach of estimating significance based on just the highest bin will not suffice. As it will not include the contribution from all the QPO bins it will fail to capture the true significance estimate. Therefore, we devise an approach that can account for multiple frequency bins. The steps are as follows:

1. After establishing that AT2018cow’s soft X-ray variability, on timescales of 1/256 Hz to 1024 Hz is white, i.e., frequency-independent, we generate a set of 105 256-s “simulated” light curves by simply randomly shuffling each observed light curve independently. In practice (in `Python`) this is done using `numpy`’s `random.shuffle` function.
2. Then we extracted an “simulated” average PDS from these shuffled light curves and rebinned it to a frequency resolution of 8 Hz just like the real PDS in Fig. 1.
3. We then searched for a QPO within this simulated average PDS at all frequencies, i.e., we fit a constant and a constant + a Lorentzian model with the centroid constrained to the ends of each frequency bin and the width allowed to be free, and computed an array of  $\Delta\chi^2$  values.
4. Finally, we record the maximum  $\Delta\chi^2$  value from the array of  $\Delta\chi^2$  value from step 3

The above steps were repeated  $10^5$  times to get an array of  $10^5$  maximum  $\Delta\chi^2$  values. We used 8 cores on a laptop for these simulations which took a total of roughly 180 hours for

442  $10^5$  simulations. From these measurements we computed the probability to exceed a certain  
443  $\Delta\chi^2$  value, i.e., 1-CDF. This is shown in the right panel of Fig. 1. For guidance, the 99.73%  
444 and 99.99% confidence levels are indicated. The QPO found in *NICER* data is statistically  
445 significant at roughly  $2 \times 10^{-4}$  level which translates to  $3.7\sigma$  equivalent for a normal distribution.

## 446 **2.3 Ruling out an instrumental and a non-astrophysical origin**

447 All *NICER* events have two types of pulse height amplitude (PHA) data: the “slow” PHA  
448 derived from the slow chain electronics and the “fast” PHA (PHA\_FAST) derived by the fast  
449 chain electronics. The standard *NICER* calibration scripts convert this information into pulse  
450 invariant (PI) and PI\_FAST, respectively. For events with energies  $\lesssim 600$  eV the fast-chain is not  
451 triggered and thus PI\_FAST is undefined. Although *NICERs* XTI is a non-imaging instrument,  
452 there is a way to separate the background (particles, cosmic X-rays, and low-energy/optical  
453 light loading events) and the source events using the values of PI and PI\_FAST. The X-ray events  
454 from an on-axis astrophysical source, high-energy particles, light loading, and the cosmic X-ray  
455 background occupy a separate region of the PI vs PI\_RATIO (PI/PI\_FAST) plot<sup>§</sup>.

456 To ensure the detected signal does not originate from any of these three types of background,  
457 we extracted an average PDS of all three backgrounds using their corresponding events within  
458 the GTIs. There was no evidence of a variability enhancement around 225 Hz (or elsewhere) in  
459 any of these three backgrounds (see Fig. S4). We describe each of these analyses in a bit more  
460 detail below.

### 461 **2.3.1 The signal is not present in the particle background**

462 High energy particles from space can interact with the silicon material in *NICER*/XTIs SDDs to  
463 produce charge and mimic X-ray events. These particle events are registered as enhancements  
464 in the so-called overshoot rate for each FPM. Also, because particles have energies much higher  
465 than *NICERs* nominal bandpass of 0.25-12 keV their incidence is also evident in the 13-15 keV  
466 count rate. Thus, if this QPO signal were from background particle events it would also be  
467 present in the overshoot and the 13-15 keV data.

468 We extracted the overshoot only event lists using the *NICER* data reduction pipeline de-  
469 scribed above but with a modified event flag `EVENT_FLAG=bxxx01x`. This particular choice  
470 selects only the overshoot events. Then, similar to our analysis on source events, we applied  
471 barycenter correction on these unfiltered (but calibrated) events. Because overshoots do not  
472 contain a PI value they cannot be energy calibrated like real X-ray events. We then extracted  
473 the average PDS using only the events within the standard GTIs (see the top-left panel of Fig.  
474 S4). There is no evidence for an excess variability anywhere in the PDS.

475 High-energy events with energies in between 13 and 15 keV that includes the *trumpet* and  
476 all PI RATIOS were extracted using the standard *NICER* tools. Then they were barycenter-  
477 corrected using the `barycorr` tool similar to the source events. The average PDS from these

---

<sup>§</sup>[https://heasarc.gsfc.nasa.gov/docs/nicer/mission\\_guide/](https://heasarc.gsfc.nasa.gov/docs/nicer/mission_guide/)

478 events is shown in the top-right panel of Fig. S4 and does not show any obvious QPO like  
479 features anywhere in the considered frequency range.

480 The average count rate of the overshoots and the 13-17 keV were 18.7 and 0.18 counts/sec,  
481 respectively. The former value is much higher than AT2018cow’s mean soft X-ray count rate  
482 of 2.62 counts/s. Therefore, if the 225 Hz QPO were from background particles it would have  
483 shown up in the top-left panel of Fig. S4 (sensitivity towards a QPO increases linearly with  
484 count rate (40)). Thus, the top two panels of Fig. S4 allows us to rule out a particle background  
485 origin for the 225 Hz QPO.

### 486 **2.3.2 The signal is not due to optical light leak events**

487 Optical light, either directly from the Sun or bright Earth at low angles, or from reflections off  
488 ISS surfaces can make its way into the FPMs. This manifests as a noise peak in each FPM whose  
489 energy spectrum peaks at an energy below 0.25 keV. However, when this light loading, which is  
490 time variable, is strong, the tail end of the noise distribution can leak into higher energies (>0.25  
491 keV) and contaminate the source events. This effect is especially important for faint targets like  
492 AT2018cow. The event filtering described in section 1.1 should already remove epochs of high  
493 light loading. To further ensure that the QPO signal is not a result of variability of “light leak”  
494 events, if any, we extracted a 0.0-0.2 keV PDS. Similar to the inband PDS we first extracted  
495 the 0.0-0.2 keV events using the standard *NICER* tasks. We then barycenter-corrected them and  
496 then computed an average PDS using events within the standard GTIs. The resulting power  
497 spectrum shown in the bottom-left panel of Fig. S4 allows us to rule out a light leak origin for  
498 this QPO.

### 499 **2.3.3 The signal is not present in cosmic X-ray background events within *NICER*’s FoV**

500 Although *NICER*/XTI is a non-imaging instrument, it’s design with the slow and the fast chain  
501 electronics allows us to separate on-axis events from the off-axis ones. While the on-axis  
502 events make a “Trumpet”-like cluster in the PI vs PI\_RATIO plot, the off-axis events, i.e., those  
503 from cosmic X-rays and other point sources in the FoV, fall above the “Trumpet”. If the QPO  
504 signal is associated with AT2018cow (placed on-axis during each observation) then it should  
505 not be present in the trumpet-rejected events. The inband PDS shown in Fig. 1 already ex-  
506 cludes trumpet-reject events. However, to be absolutely sure, we extract an average PDS of the  
507 trumpet-rejected events within the standard GTIs. We extracted the trumpet-rejected events by  
508 first extracting the standard cleaned event lists with `trumpfilt=NO`. These were barycenter-  
509 corrected and then screened to only include events between 0.25 and 10 keV that fell above the  
510 trumpet edge defined by the curve  $PI\_RATIO = 1.1 + 120/PI$ . An average PDS was extracted in  
511 same manner as the inband PDS. This is shown in the bottom-right panel of Fig. S4 and it is  
512 evident that a 225 Hz QPO is not present in events that describe the cosmic X-ray background  
513 and any contaminating sources in the field of view.

#### 514 **2.3.4 The signal is present in all Measurement and Power Units (MPUs)**

515 If this signal is astrophysical in origin then it must be uniformly distributed across all the 52  
516 active FPMs which are controlled by 7 MPUs<sup>¶</sup>. We checked to ensure that is the case by  
517 extracting several average PDS, but with data from one MPU removed at a time. The resulting 7  
518 PDS with the ID of the removed MPU at the top are shown in Fig. S5. The QPO is evident in all  
519 the 7 PDS with a fractional rms amplitude value consistent with each other. This demonstrates  
520 that the QPO events are uniformly distributed across all MPUs and not just limited to any single  
521 unit.

#### 522 **2.3.5 The signal is not due to “GPS” noise**

523 One other plausible instrument-related source of origin of this signal is the co-called “Global  
524 Position System (GPS) noise. During the ground testing of *NICER*s MPUs anomalous cross-talk  
525 signals between the FPM input line and the GPS pulse-per-second (PPS) line were observed.  
526 This can result in certain FPMs registering pseudo events (non-cosmic) immediately following  
527 a GPS PPS tick, usually within the first 4 ms after the tick. In principle, this could produce a 1  
528 second QPO with roughly a 4 ms QPO width, although it has never been reported in any of the  
529 analysis of several *NICER* targets thus far. This is obviously at a different frequency compared  
530 to the 225 Hz QPO from observations of AT2018cow. Nevertheless, we rule out GPS noise as  
531 the source of AT2018cows QPO by first removing all events with time stamps occurring within  
532 10 ms of an integer second of the original non-barycenter corrected data. Then, we barycenter  
533 corrected the remaining events and extracted an average PDS in the exact same manner as the  
534 PDS in Fig. 1. The resulting PDS shown in Fig. S6 is virtually indistinguishable from the left  
535 panel of Fig. 1. This is not too surprising as the above only excludes a small fraction of all  
536 events. Fig. S6 shows that the signal is still present after removing the plausible GPS noise  
537 events and rules out GPS noise as the origin of this QPO.

#### 538 **2.3.6 AT2018cow dominates the X-ray emission in *NICER*/*XTI*’s FoV**

539 *NICER*/*XTI* is a non-imaging detector with a field of view of roughly 30 arcmin<sup>2</sup>. Thus it is  
540 plausible that a contaminating point source other than AT2018cow could have produced this  
541 QPO signal. To investigate this possibility, we extracted an image by stacking the entire Neil  
542 Gehrels *Swift*/*XRT* archival data of AT2018cow (see the right panel of Fig. 3). It is clear from  
543 these images that AT2018cow is the brightest point source within *XTI*’s FoV. The contribution  
544 from the other point sources is negligible.

545 Furthermore, we can directly compare *NICER*/*XTI* light curve of AT2018cow’s FoV with  
546 resolved *XRT* light curve. The variability features in *XRT* light curve are also evident in *XTI*  
547 data (see Fig. 2). This independently implies that AT2018cow dominates the X-ray emission in  
548 *XTI*’s FoV.

---

¶[https://heasarc.gsfc.nasa.gov/docs/nicer/mission\\_guide/](https://heasarc.gsfc.nasa.gov/docs/nicer/mission_guide/)

549 As a final check, we also investigated a late time *XMM-Newton* image of AT2018cow's  
550 FoV to rule out contamination by a point source within XRT or EPIC instrument's point spread  
551 functions. The left panel of Fig. 3 show MOS1 image of AT2018cow's FoV at late times. We  
552 used MOS1 because it offers the best pixel size of 4.1". It is evident that long after AT2018cow's  
553 optical decay, there is no X-ray emission present at its location and rules out a contaminating  
554 source very close to the position of AT2018cow.

555 The combination of the above three analyses affirms that the majority of emission detected  
556 by XTI between MJD 58290.87 and 58349.11 and thus the 225 Hz signal originates from  
557 AT2018cow.

### 558 **2.3.7 A similar signal is NOT present in any AGN monitored by *NICER* during the same** 559 **epoch**

560 AGN host supermassive black holes ( $\gtrsim 10^5 M_{\odot}$ ) and hence causality argument suggests that they  
561 should not show any variability on timescales of milliseconds, i.e., hundreds of Hz. Therefore,  
562 to be absolutely sure that the 225 Hz QPO signal is unique to AT2018cow data we also extracted  
563 average PDS of 3 active galactic nuclei that *NICER* monitored during the same epoch, i.e., only  
564 using their observations between MJD 58290.87 and 58349.11. These resulting average PDS  
565 are shown in Fig. S8 and a 225 Hz feature is not seen in any of them.

## 566 **2.4 QPO is highly persistent**

567 The fact that the QPO is detected in the average PDS extracted from data accumulated over a  
568 temporal baseline of  $\approx 60$  days suggests that the QPO is likely present for a significant fraction  
569 of the X-ray monitoring. To further test this we estimated the strength (signal-to-noise ratio) of  
570 the QPO as a function of the accumulated exposure. We started with the first 5 ks of exposure,  
571 extracted an average PDS, and fit the 225 Hz feature with a Lorentzian. From thereon, for every  
572 additional 256-s exposure, we repeated this process of extracting an average PDS, followed  
573 by modelling the 225 Hz feature with a Lorentzian. At every point, the QPO strength was  
574 calculated as the ratio of the sum of the powers within the width of the best-fit QPO and its  
575 errorbar. A normalized QPO strength was also estimated by dividing the QPO strength with  
576 the average count rate which itself evolves with the accumulated exposure. It is evident from  
577 Fig. S7 that the overall strength of the QPO gradually increases with increasing exposure. This  
578 demonstrates that:

- 579 1. The QPO was persistent for a substantial fraction of the 60 d monitoring program, i.e.,  
580 for several hundreds of millions of cycles ( $\sim 60\text{days}/4.4\text{ms}$ ).
- 581 2. The QPO signal does not originate from any single exposure of the *NICER* monitoring.

582 The same result can be visualized in the form of a movie showing the evolution of the  
583 average PDS as a function of increasing exposure. This can be found as a supplementary file  
584 (Movie S1). A gif version is also available.

### 3 Implications for a magnetar scenario

The bolometric light curve of AT2018cow reached a luminosity of  $\sim 4 \times 10^{44}$  erg s $^{-1}$  on time a timescale of a few days after the explosion, and the luminosity decayed as  $L_e \propto t^{-\alpha}$ , where  $\alpha \approx 2.5$  at times,  $t \gtrsim t_e \sim 10^3 - 10^5$  s. The central engine responsible for powering the optical and X-ray emission must supply a total energy  $E_e \sim 10^{50} - 10^{52}$  erg over a characteristic timescale of  $t_e$ . Degeneracy exists in these properties because we do not know how much of the kinetic energy of the ejecta is supplied by the initial explosion itself, versus injected at later times by the engine.

Two models for the central engine include: (1) a stellar-mass black hole of mass  $\sim 10\text{-}30M_\odot$  created by the failed explosion of a very massive star, which is accreting fall-back material from the outer layers of the extended progenitor at a highly super-Eddington rate; (2) a magnetar with a rapid birth period  $P_0 \sim$  ms and a strong dipole magnetic field  $B \sim 10^{14}\text{-}10^{15}$  G. The magnetar may be spinning down in isolation, or it may be accreting fall-back material as in the black hole. The latter scenario may be supported by the predict decline rate of the engine luminosity  $L_e \propto t^{-2.38}$ .

We now consider models for the origin of the QPO-like feature at  $f_{\text{QPO}} = 225$  Hz, assuming it is related to the spin period of a magnetar,  $P_{\text{QPO}} = 1/f_{\text{QPO}} \approx 4.44$  ms or half of that value ( $P_{\text{QPO}} = 8.9$  ms). Alternatively, the QPO could arise directly in the accretion disk (of the black hole or neutron star), e.g. as in an X-ray binary QPO, a possibility which is not addressed below.

#### 3.1 Spin of an isolated pulsar or magnetar

Here we consider the possibility that the observed QPO at 225 Hz is the spin frequency of a pulsar or magnetar. The traditional picture of pulsar spin evolution (see, e.g., (42), for a review) is that the pulsar's rotational energy

$$E_{\text{rot}}(\nu) = \frac{I}{2} (2\pi\nu)^2 \sim 1 \times 10^{51} \text{ erg} \left( \frac{\nu}{225 \text{ Hz}} \right)^2, \quad (\text{S1})$$

where  $I \sim 10^{45}$  g cm $^2$  is the stellar moment of inertia, can supply energy at a rate

$$L_{\text{sd}} = 4\pi^2 I \nu \dot{\nu} \sim 3 \times 10^{43} \text{ erg s}^{-1} \left( \frac{\nu}{225 \text{ Hz}} \right) \left( \frac{\dot{\nu}}{3 \times 10^{-6} \text{ Hz s}^{-1}} \right) \quad (\text{S2})$$

to power radiation from a rotating magnetic dipole at a rate  $L_{\text{mag}} \propto B^2 \nu^4$ . Equating the two rates yields an estimate of the pulsar magnetic field

$$B \approx 2 \times 10^{13} \text{ G} \left( \frac{\nu}{225 \text{ Hz}} \right)^{-3/2} \left( \frac{-\dot{\nu}}{3 \times 10^{-6} \text{ Hz s}^{-1}} \right)^{1/2} \quad (\text{S3})$$

611 and evolution of spin frequency

$$\nu = \nu_0(1 + t/t_{\text{sd}})^{-1/2}, \quad (\text{S4})$$

612 which then leads to

$$L_{\text{sd}} = \frac{E_{\text{rot}}(\nu_0)}{t_{\text{sd}}} \frac{1}{(1 + t/t_{\text{sd}})^2} = \frac{3 \times 10^{43} \text{ erg s}^{-1}}{(1 + t/t_{\text{sd}})^2} \left( \frac{\nu_0}{225 \text{ Hz}} \right) \left( \frac{-\dot{\nu}_0}{3 \times 10^{-6} \text{ Hz s}^{-1}} \right), \quad (\text{S5})$$

613 where the characteristic timescale for spin-down is

$$t_{\text{sd}} = -\frac{\nu_0}{2\dot{\nu}_0} \approx 430 \text{ d} \left( \frac{\nu_0}{225 \text{ Hz}} \right) \left( \frac{-\dot{\nu}_0}{3 \times 10^{-6} \text{ Hz s}^{-1}} \right)^{-1} = 430 \text{ d} \left( \frac{\nu_0}{225 \text{ Hz}} \right)^{-2} \left( \frac{B}{2 \times 10^{13} \text{ G}} \right)^{-2} \quad (\text{S6})$$

614 and  $\nu_0$  and  $\dot{\nu}_0$  are the initial spin frequency and spin frequency time derivative, respectively.  
 615 One can see from equation (S5) that the luminosity is constant at times  $t \ll t_{\text{sd}}$  and decreases  
 616 as  $L_{\text{sd}} \propto t^{-2}$  when  $t \gg t_{\text{sd}}$ .

617 The QPO in AT2018cow is observed to persist at 225 Hz for about 60 days with a width of  
 618  $< 16$  Hz. This constrains the frequency change to

$$|\dot{\nu}| < 16 \text{ Hz}/60 \text{ d} = 3 \times 10^{-6} \text{ Hz s}^{-1} \quad (\text{S7})$$

619 and magnetic field and spin-down timescale to  $B < 2 \times 10^{13} \text{ G}$  and  $t_{\text{sd}} > 430 \text{ d}$ , respectively.  
 620 Even stricter constraints of

$$-\dot{\nu} < 3 \times 10^{-8} \text{ Hz s}^{-1} \left( \frac{L}{3 \times 10^{41} \text{ erg s}^{-1}} \right) \quad (\text{S8})$$

621 and  $B < 2 \times 10^{12} \text{ G}$  ( $L/3 \times 10^{41} \text{ erg s}^{-1}$ )<sup>1/2</sup> are obtained from equations (S3) and (S5) by  
 622 noting that the bolometric and X-ray luminosities are seen to decrease at times  $< 60 \text{ d}$  to a  
 623 lowest value of  $\sim 10^{41} \text{ erg s}^{-1}$  (5).

624 The above discussion rules out the possibility of a millisecond magnetar powering AT2018cow.  
 625 If  $B > 10^{14} \text{ G}$ , then  $t_{\text{sd}} < 20 \text{ d}$  and  $-\dot{\nu} > 1 \times 10^{-4} \text{ Hz s}^{-1}$ . The latter in particular implies the  
 626 QPO frequency would have decreased by more than 100 Hz in a span of just 10 days.

## 627 3.2 Neutron star accretion

628 Alternatively, a remnant magnetar may be accreting fall-back matter from its birthing supernova  
 629 explosion, and the observed engine activity is either accretion or spin-down powered. The rate  
 630 of mass fall-back can be written (e.g., (43))

$$\dot{M}(t) = \frac{2 M_{\text{acc}}}{3 t_{\text{acc}}} \frac{1}{(1 + t/t_{\text{acc}})^{5/3}}, \quad (\text{S9})$$

631 where  $M_{\text{acc}}$  is the total quantity of returning mass and  $t_{\text{acc}} \sim t_{\text{ff}} \sim (G\bar{\rho})^{-1/2}$  is the characteristic  
632 fall-back time which depends on the mean density  $\bar{\rho}$  of the layer of progenitor star contributing  
633 to  $M_{\text{acc}}$ . For an extended star with hydrogen-rich ejecta like a blue supergiant ( $\bar{\rho} \sim 10^{-5} - 10^{-3}$   
634  $\text{g cm}^{-3}$ ), we have  $t_{\text{acc}} \sim 10^5 - 10^6$  s, compatible with the timescale of engine activity for  
635 AT2018cow (5). A neutron star of initial mass  $M_{\text{ns}} \approx 1.4M_{\odot}$  can accrete at most  $M_{\text{acc}} \approx$   
636  $0.8M_{\odot}$  before collapsing into a black hole and thus indicates a maximum accretion rate in the  
637 range  $\lesssim 10^{-6} - 10^{-5}M_{\odot} \text{ s}^{-1}$ , i.e., 9-10 orders of magnitude above the Eddington accretion  
638 rate for a solar-mass compact object. By comparison, to explain the peak engine luminosity of  
639 AT2018cow ( $\sim 10^{45} \text{ erg s}^{-1}$  or 7 orders of magnitude above the Eddington luminosity) through  
640 accretion would require either a lower peak accretion rate  $\dot{M} \sim 10^{-8}M_{\odot} \text{ s}^{-1}$  or inefficient  
641 production of X-rays by the accretion flow. On timescales of several weeks, relevant to the  
642 epoch of the observed QPO, the accretion rate is  $\sim 2$  orders of magnitude lower than at peak,  
643 i.e. in the characteristic range

$$\dot{M}(t_{\text{QPO}}) \sim 10^{-10} - 10^{-8}M_{\odot}\text{s}^{-1} \quad (\text{S10})$$

644 The Alfvén radius of the accretion flow, at which the ram pressure of the incoming flow is  
645 balance by magnetic forces, is given by (e.g., (43))

$$R_A \approx 40B_{12}^{4/7}\dot{M}_{-9}^{-2/7}M_{1.4}^{-1/7} \text{ km}, \quad (\text{S11})$$

646 where  $\dot{M}_{-9} = \dot{M}/(10^{-9} M_{\odot} \text{ s}^{-1})$  and now we have normalized the surface magnetic field  $B_{12} =$   
647  $B/10^{12} \text{ G}$  to a lower value more akin to a radio pulsar than a magnetar. If the magnetic field is  
648 sufficiently large that  $R_A$  exceeds the neutron star radius  $\approx 12 \text{ km}$ , i.e. if

$$B_{12} \gtrsim 0.1\dot{M}_{-9}^{1/2}M_{1.4}^{1/4}, \quad (\text{S12})$$

649 then the accretion flow will be directed from the disk onto the magnetic axis of the neutron star,  
650 providing a possible mechanism to induce periodicity in the signal on the rotation period.

651 In order for accretion to occur, a neutron star must rotate slow enough that it is not in an  
652 ejector phase (44–46), and this occurs approximately when the Alfvén radius  $R_A$  is smaller than  
653 the light cylinder radius  $R_{\text{lc}} \equiv c/2\pi\nu$ . This then implies

$$B_{12} < 20\dot{M}_{-9}^{1/2}M_{1.4}^{1/4} \left( \frac{\nu}{225 \text{ Hz}} \right)^{-7/4}. \quad (\text{S13})$$

654 Accretion also affects the spin-down rate of the neutron star, driving the spin-period to an

655 equilibrium value given by (43, 45, 47, 48)<sup>||</sup>

$$P_{\text{eq}} \approx 4 B_{12}^{6/7} \dot{M}_{-9}^{-3/7} M_{1.4}^{-5/7} \text{ ms} \quad (\text{S14})$$

656 Explaining the observed QPO ( $P_{\text{eq}} \approx 1 - 2P_{\text{QPO}} \approx 4.4 - 8.8$  ms) thus requires an accretion  
657 rate of

$$\dot{M}(t_{\text{QPO}}) \approx (2 - 9) \times 10^{-10} B_{12}^2 M_{1.4}^{-5/3} M_{\odot} \text{ s}^{-1}, \quad (\text{S15})$$

658 consistent with our estimate in eq. S10. However the timescale to reach this equilibrium  
659 (Ref. (43), their eq. 21; see also (45–47, 50)),

$$\tau_{\text{eq}} \approx 400 \text{ d } B_{12}^{-8/7} \dot{M}_{-9}^{-3/7} M_{1.4}^{16/7} \underset{\dot{M}=\dot{M}_{\text{QPO}}}{\approx} (400 - 900) B_{12}^{-2} M_{1.4}^{16/7} \text{ d} \quad (\text{S16})$$

660 can be long. This indicates that  $P \approx P_{\text{eq}}$  will only be achieved on timescales of the observed  
661 QPO ( $\tau_{\text{eq}} \ll 25 \text{ d}$ ) if  $B$  (or, equivalently,  $\dot{M} \propto B^2$ ) is sufficiently high,  $B_{12} \gtrsim 3$ . In such a case  
662 that  $\tau_{\text{eq}} \gg t_{\text{QPO}}$ , then the spin period would reflect that of the neutron star at birth rather than  
663  $P_{\text{eq}}$ , the equilibrium value achieved through accretion.

664 In this scenario, if  $P = P_{\text{eq}}$  is achieved, then the rotation period of the neutron star (and  
665 thus the QPO frequency) should increase in time as (eq. S14)

$$P_{\text{eq}} \propto \dot{M}^{-3/7} \underset{\dot{M} \propto t^{-5/3}}{\propto} t^{5/7}, \quad (\text{S17})$$

666 somewhat faster than in the isolated magnetar case (eq. S4).

667 One appealing aspect of this scenario is that, again if the equilibrium  $P = P_{\text{eq}}$  is achieved,  
668 then the luminosity of the neutron star wind is given by (Ref. (43), their eq. 22)

$$L_{\text{sd}} \approx 1 \times 10^{43} B_{12}^{-6/7} \dot{M}_{-9}^{10/7} M_{1.4}^{12/7} \text{ erg s}^{-1} \underset{\dot{M}=\dot{M}(t_{\text{QPO}})}{\approx} (10^{42} - 10^{43}) B_{12}^2 \text{ erg s}^{-1}, \quad (\text{S18})$$

669 similar to the luminosity of AT2018cow on timescales of a few weeks. Furthermore, if  $\dot{M} \propto$   
670  $t^{-5/3}$  then one predicts a decay in the luminosity  $L_{\text{sd}} \propto \dot{M}^{10/7} \propto t^{-2.38}$ , close to the observed  
671 decay of the bolometric light curve of AT2018cow (e.g., (5)).

672 This is comparable to the accretion power onto the neutron star surface,

$$L_{\text{acc}} \approx \frac{GM_{\text{ns}} \dot{M}}{R_{\text{ns}}} \approx 3 \times 10^{44} \dot{M}_{-9} M_{1.4} \text{ erg s}^{-1} \underset{\dot{M}=\dot{M}_{\text{QPO}}}{\approx} 3 \times 10^{42} - 2 \times 10^{43} B_{12}^2 \text{ erg s}^{-1}, \quad (\text{S19})$$

673 which could therefore also contribute to the luminosity. However, given the generally low ra-  
674 diative efficiency of highly super-Eddington accretion flows, its contribution could be swamped

---

<sup>||</sup>Unlike in some past work, we assume that this equilibrium is determined by the balance of accretion spin-up and spin-down from the magnetized wind (the latter enhanced as a result of the larger magnetosphere opened by the fall-back (49)).

675 by energy injected from the neutron star wind,  $L_{sd}$ .

676 Even with the narrow range of 200-250 Hz the search space for the pulsar (frequency, start  
677 time of the explosion) is rather large. We defer the search for the pulsar to a future work as it  
678 requires significant computational resources on a computer cluster unavailable to the authors  
679 at present. But we provide the barycenter corrected events as supplementary files so that any  
680 reader with access to such a cluster may use it. A sample Python code to load all the events is  
681 also provided (`load_events.py`).

## 682 4 Pulsation search assuming a binary

683 To search for possible orbital periodicities, we used the open source PRESTO software\*\* to  
684 perform an acceleration search over the frequency-frequency derivative plane. The acceleration  
685 search scheme assumes that the compact objects acceleration is roughly constant throughout the  
686 observation of duration  $T \lesssim P_{orb}/10$  (51). We ran the search assuming that any possible signal  
687 would drift across a maximum of 100 Fourier frequency bins ( $zmax$  of 100). Informed by the  
688 centroid frequency and width of the QPO (assumed to be the fundamental frequency) reported  
689 above, we narrowed the search frequency window to be over 200-260 Hz<sup>††</sup>. The acceleration  
690 search yielded no candidates above 3 sigma (single trial probability). Subsequently, we ac-  
691 counted for the possibility of linearly changing accelerations, and carried out a jerk search (52),  
692 with PRESTO<sup>‡‡</sup>. This opens the way to detect other more exotic systems like very compact,  
693 relativistic binary systems, and allows searches over longer observations, unlike in acceleration  
694 searches. The jerk search would also allow us to recover any lost signal from residual Doppler  
695 smearing in the previous acceleration searches (53). In the end, the jerk search also yielded no  
696 candidates above 3 sigma (single trial probability).

697 As described in section 3, the spin of the potential neutron star will evolve in a manner  
698 that depends strongly on the actual underlying physical scenario. Exploring all these models is  
699 beyond the scope of this work.

---

\*\* <https://github.com/scottransom/presto>

†† in PRESTO parlance, this is *flo* of 200, and *fhi* of 260

‡‡ In PRESTO parlance, this is *wmax* of 300

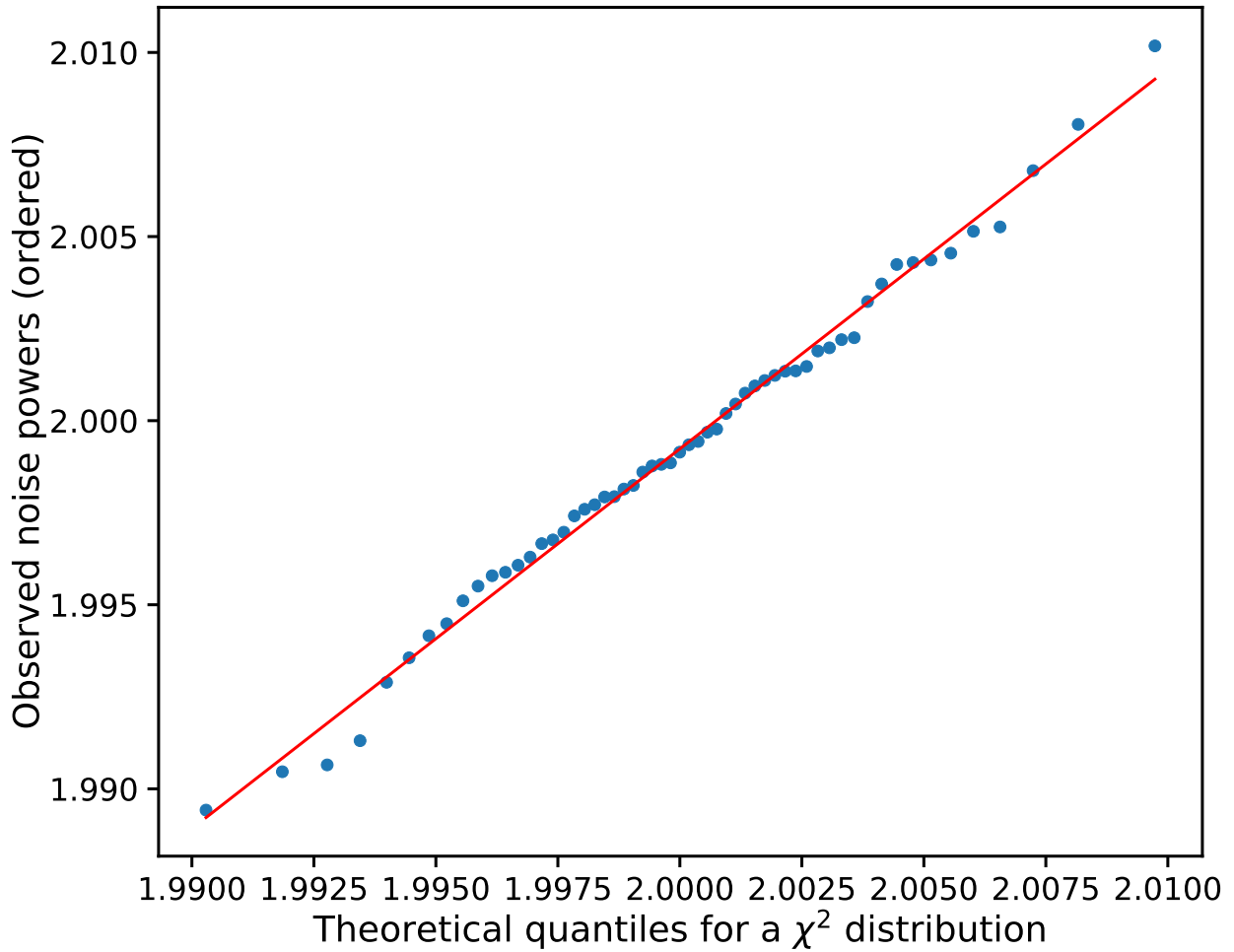


Figure S1: **Probability plot to visually assess whether the power values in the PDS continuum are  $\chi^2$  distributed.** This is a *qualitative* assessment tool that tells us that if the data points lie on a straight line, as they do, they appear consistent with the theorized model, which in the present case is a  $\chi^2$  distribution with  $2 \times 105 \times 2048$  degrees of freedom (see section 2.2.1 for more details).

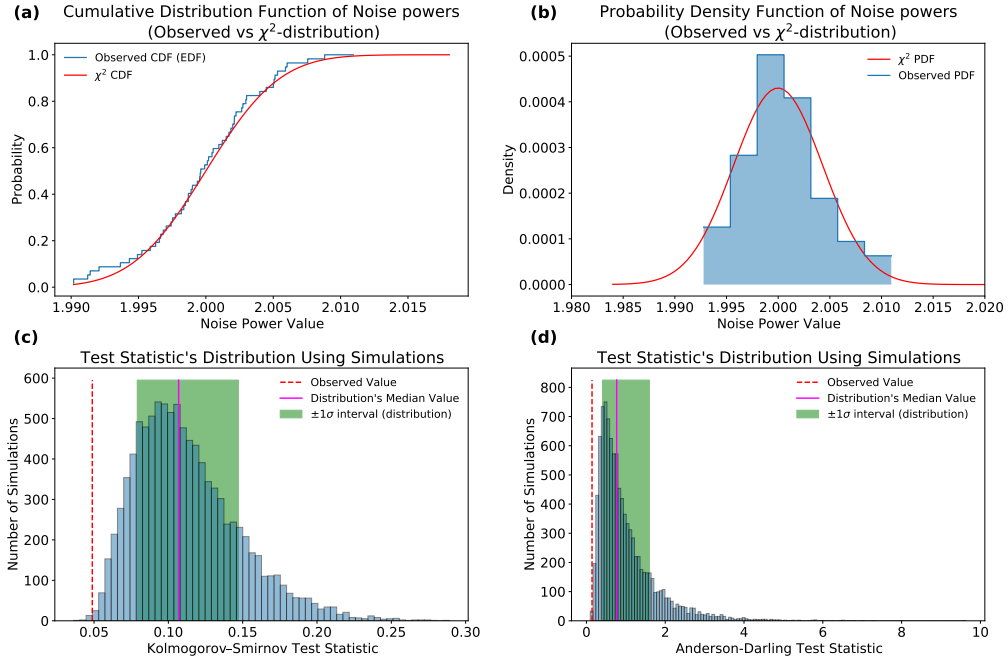


Figure S2: **White noise tests for soft X-ray PDS of AT2018cow.** *Top-left:* Comparing the empirical distribution function (EDF) of the values in the PDS continuum (blue histogram) with the cumulative distribution function of a  $\chi^2$  distribution with  $2 \times 105 \times 2048$  degrees of freedom. *Top-right:* Comparison of the observed probability distribution function (PDF) with the expected PDF of a  $\chi^2$  distribution with  $2 \times 105 \times 2048$  dof. Both the observed PDF and EDF track expected curves quite well. *Bottom-left:* The distribution of the K-S statistic derived from EDFs sampled from a  $\chi^2$  distribution with  $2 \times 105 \times 2048$  dof. *Bottom-right:* Same as *bottom-left* but using an Anderson-Darling test statistic. Both the test statistic values are consistent with a  $\chi^2$  distribution and suggest that the PDS continuum is white (see section 2.2.2 for more details).

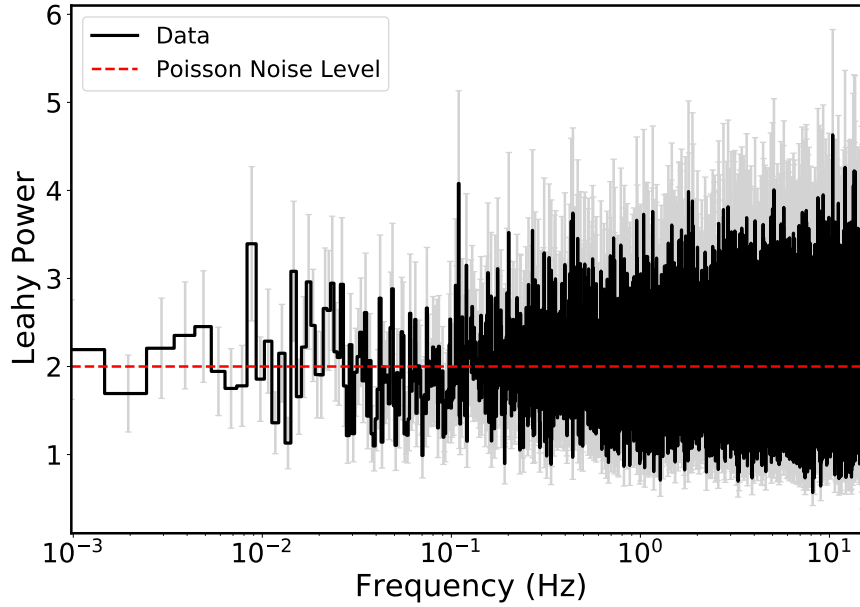


Figure S3: *XMM-Newton/EPIC-pn* soft X-ray (0.25-2.5 keV) PDS of AT2018cow to assess noise continuum at low frequencies. The PDS was derived by averaging 15 1024 s light curve segments sampled at 1/16 Hz. The frequency resolution is 1/2048 Hz. It is evident that even at frequencies as low as 1/2048 Hz there is no evidence for red noise. The 225 Hz QPO in *NICER* data is outside of this band pass, i.e., beyond EPIC-pn's Nyquist frequency.

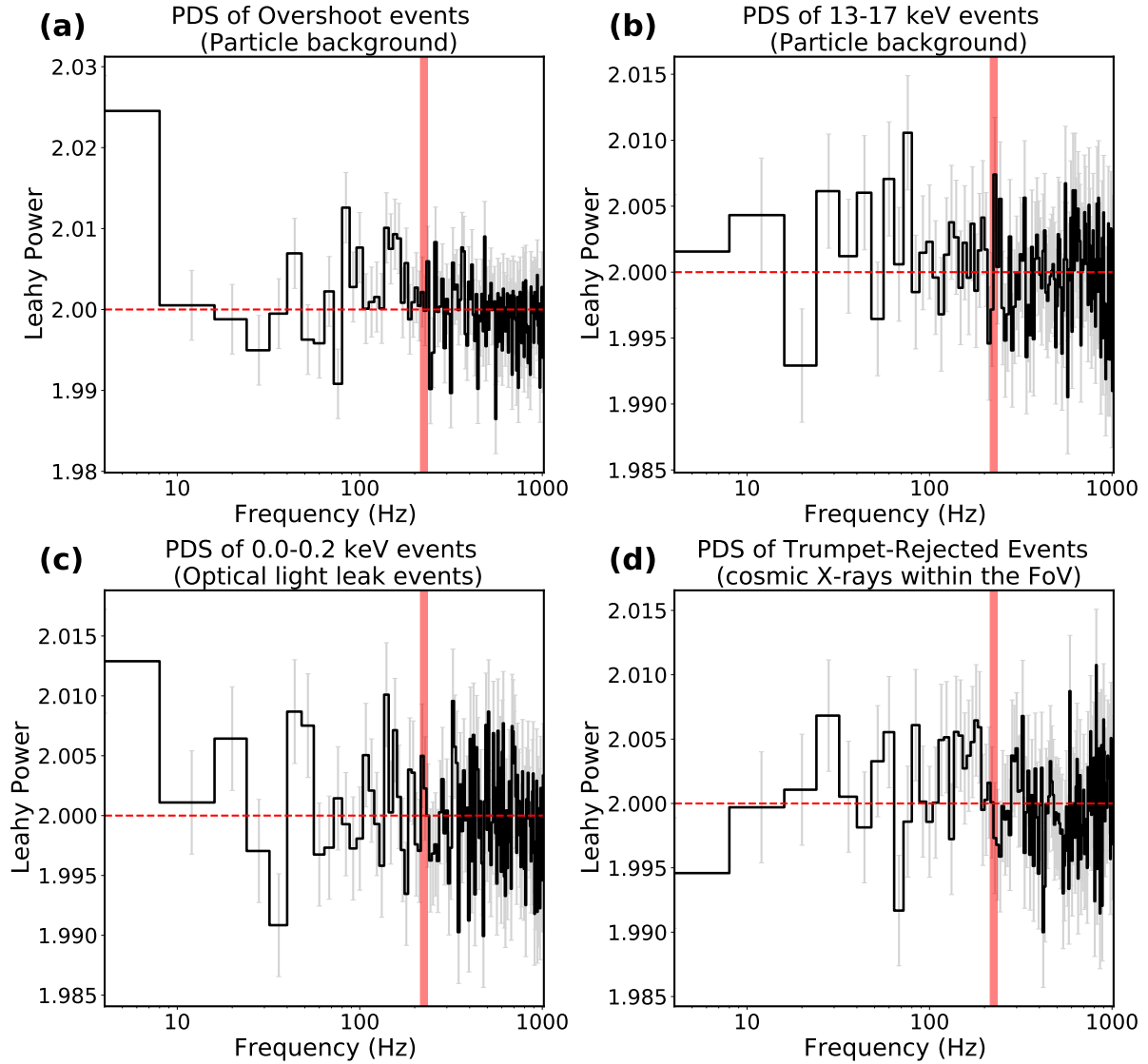


Figure S4: *NICER* PDS of various types of noise. (a) and (b) show the PDS of the overshoots and the 13-15 keV events, respectively. They both track the particle background. (c) The average PDS of 0.0-0.2 keV events. These are the optical light leak events. (d) The average PDS derived from trumpet-rejected events. These are the off-axis events that track the cosmic X-ray and other sources in the FoV. In all cases, the frequency resolution, the number of spectra averaged and the frequency rebinning is same as the left panel of Fig. 1. The red shaded rectangle shows the location of the 225 Hz QPO. Clearly, there is no statistically significant evidence for a 225 Hz QPO in any of these noise power spectra. The dashed horizontal line indicates the expected Poisson noise level of 2. These plots suggest that the 225 Hz QPO in Fig. 1 does not originate from any of these background events.

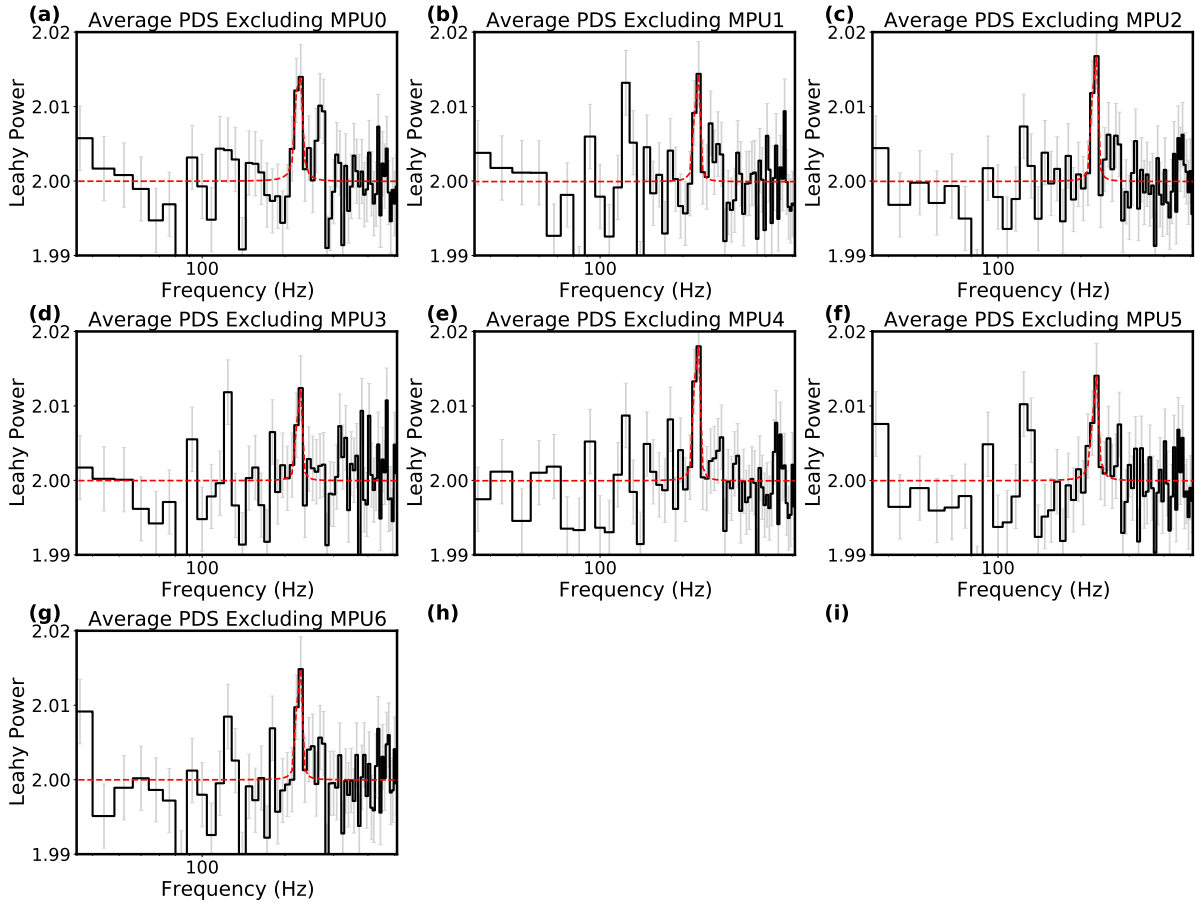


Figure S5: *NICER* power spectra with one MPU removed at a time. The QPO properties, i.e., fractional rms strength, centroid and width are all same (within errorbars) across all the above PDS. This demonstrates that the QPO signal is uniformly distributed across all the MPUs and points towards an non-instrumental origin.

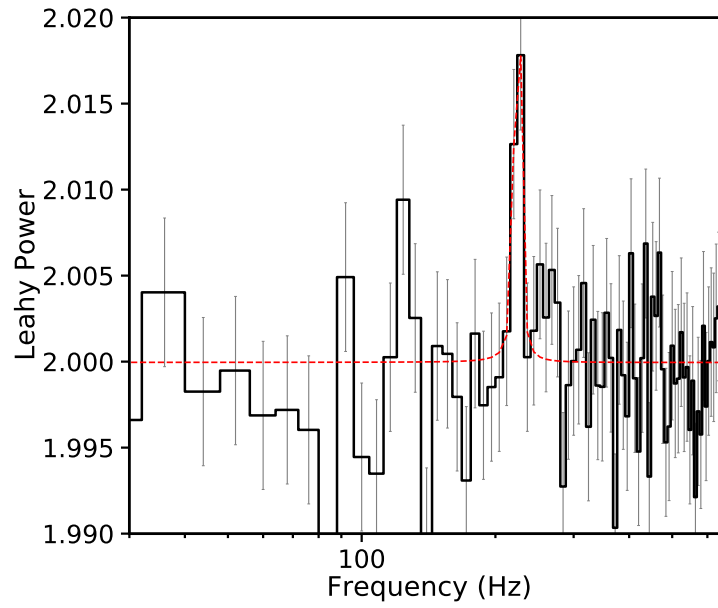


Figure S6: **Same power spectra as the left panel of Fig. 1 but with plausible GPS noise events removed.** This PDS is indistinguishable from Fig. 1 and demonstrates that the GPS noise, if any, is not the origin of the 225 Hz QPO (see section 2.3.5 for more details)

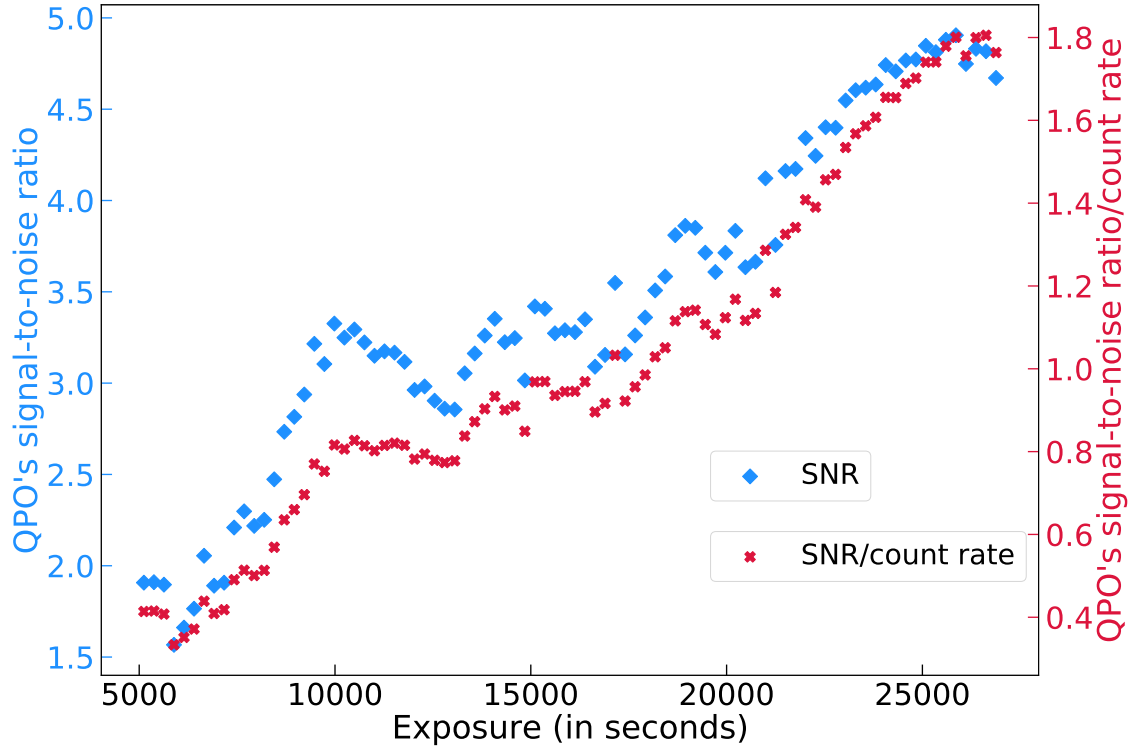


Figure S7: **QPO's signal-to-noise ratio (blue diamonds) and signal-to-noise over average count rate (red crosses) vs accumulated exposure time.** It is evident that the QPO's signal-to-noise gradually increases with increasing exposure. This suggests that the signal is persistent throughout the *NICER* monitoring period and it does not originate from any single exposure. The steepening of the mean slope around 20000 s corresponds to day 17. Note that the data points are not independent (see sec. 2.4 for more details). See also supplement movie S1. Data available in supplementary files.

700 **Movie S1:** The top panel of the movie shows the evolution of the average PDS and the gradual  
701 improvement in the QPO signal at 225 Hz with accumulated exposure. The lower panel shows  
702 the corresponding long-term light curve. The shaded red rectangle in the top panel shows the  
703 location of the 225 Hz QPO. This suggests that the QPO is long-lived and present in majority  
704 of the observations. This is available as *Movie\_S1.gif*.

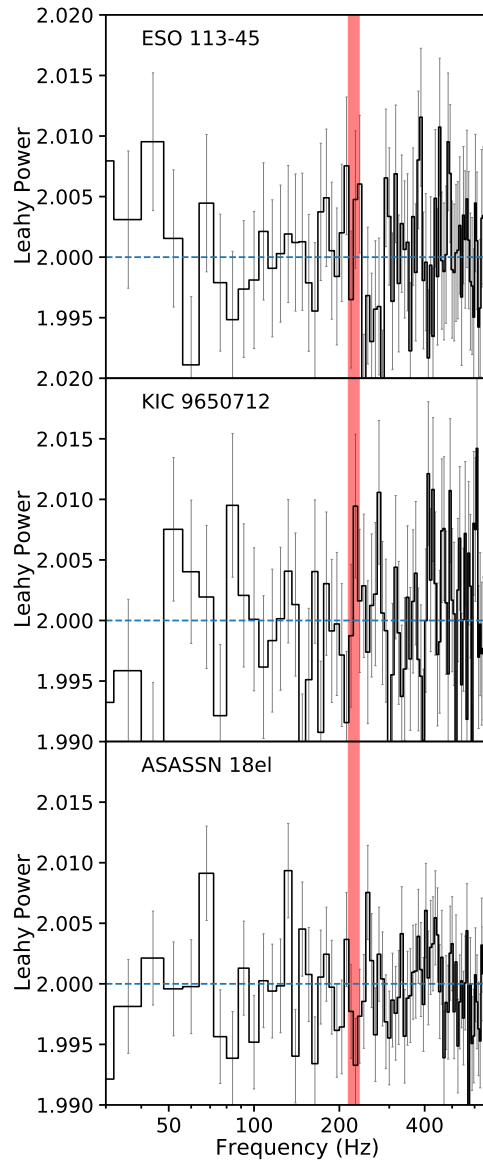


Figure S8: **Average PDS of 3 AGN monitored by *NICER* during the same 2 month period as AT2018cow.** The AGN names are shown on each panel. The mean count rates (exposures) (from top to bottom) are 30.5 (15.6 ks), 3.9 (14.3 ks) and 1.2 (33.3 ks) counts/s, respectively. These PDS were extracted exactly the same way as the average PDS of AT2018cow in Fig. 1. The location of AT2018cow's QPO is indicated by the red shaded area. There is no evidence for a 225 Hz QPO in any of these power spectra. This provides further support that the 225 Hz QPO in Fig. 1 is intrinsic to AT2018cow's data.

# Figures

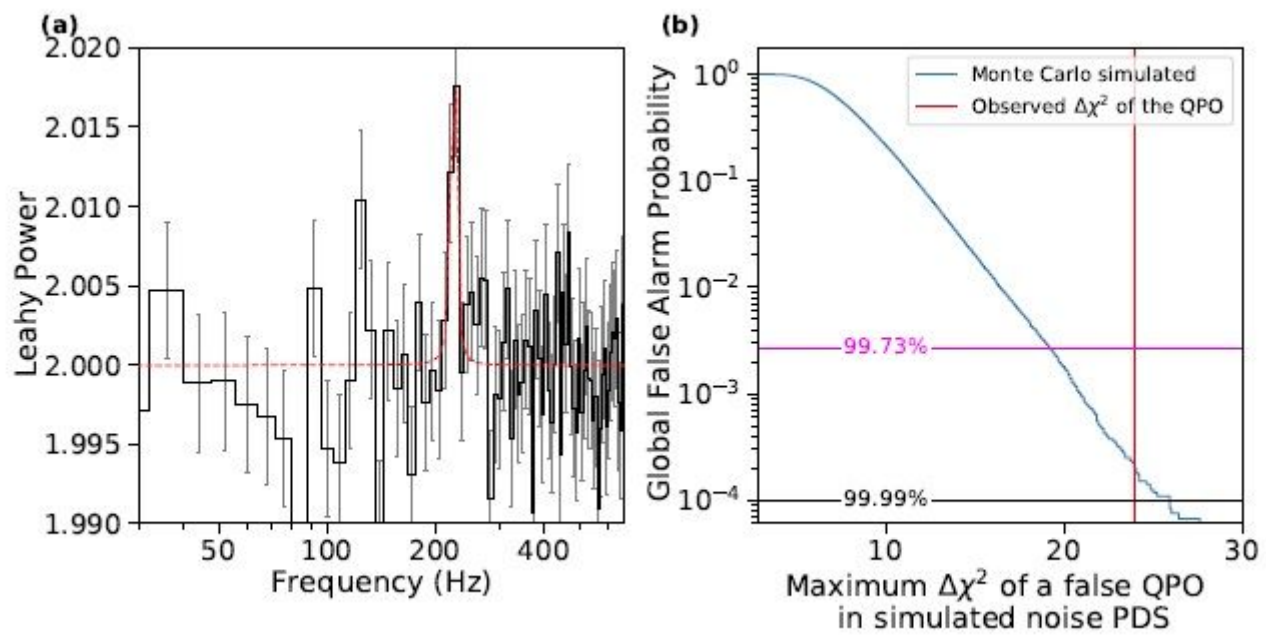


Figure 1

(see Manuscript file for figure caption)

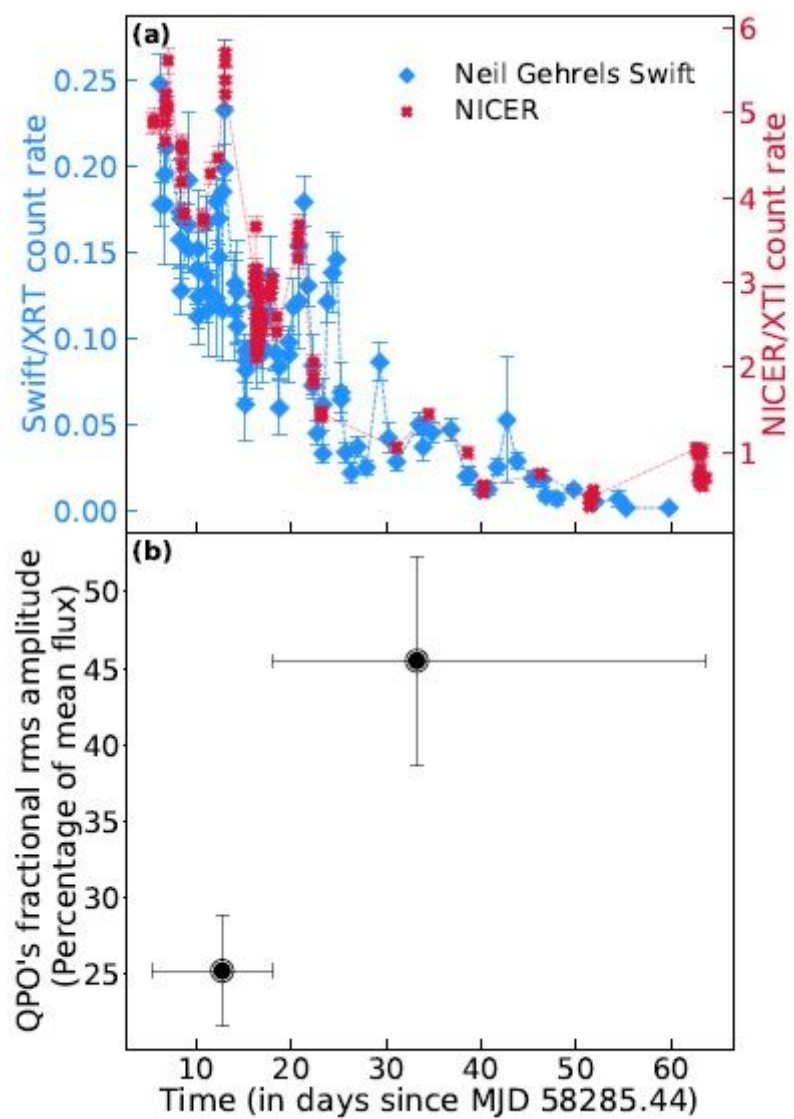
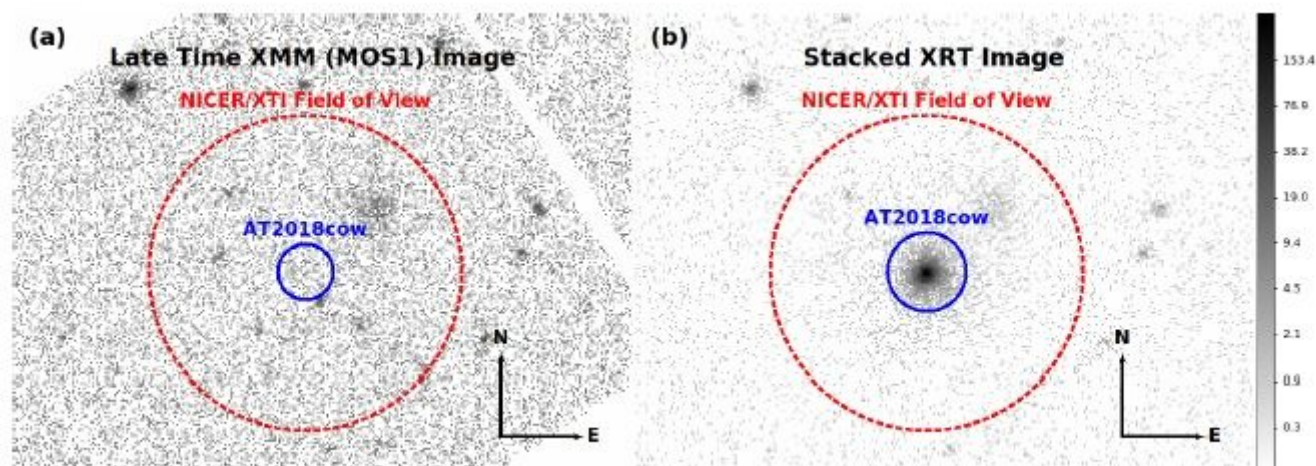


Figure 2

(see Manuscript file for figure caption)



## Figure 3

(see Manuscript file for figure caption)

## Supplementary Files

This is a list of supplementary files associated with this preprint. Click to download.

- [MovieS1.gif](#)